Dissertation

Physical/chemical methods for SARS-CoV-2 inactivation

Submitted by

Stella Annamaria Isabel Wolfgruber BSc MSc

For the Academic Degree of

Doctor of Medical Science

at the

Medical University of Graz

Diagnostic and Research Institute of Pathology

Under the supervision of

Univ. Prof. I.R. Dr. Kurt Zatloukal

2025

Declaration

I hereby declare that this dissertation is my own original work. I have fully acknowledged by name all individuals and organizations that have contributed to the research. All other materials used have been properly cited within the text. In the preparation of this dissertation and all related publications, I have strictly followed the "Guidelines of the Medical University of Graz on Good Scientific Practice."

17.01.2025

Disclosures

Please note that parts of this thesis have already been published:

Antiviral Activity of Zinc Oxide Nanoparticles against SARS-CoV-2.

Wolfgruber Stella[1], Rieger Julia[1], Cardozo Olavo[2, 3], Punz Benjamin[4], Himly Martin[4], Stingl Andreas[2], Farias Patricia M A[2, 5], Abuja Peter M[1], Zatloukal Kurt[1]

[1] Diagnostic and Research Center for Molecular Biomedicine, Institute of Pathology, Medical University of Graz, 8010 Graz, Austria.
[2] PHORNANO Holding GmbH, Kleinengersdorferstrasse 24, 2100 Korneuburg, Austria.
[3] Post-Graduate Program on Electrical Engineering, Federal University of Pernambuco, Cidade Universitaria, Brazil.
[4] Department of Biosciences and Medical Biology, Paris Lodron University of Salzburg, 5020 Salzburg, Austria.
[5] Department of Biophysics and Radiobiology, Post-Graduate Program on Material Sciences, Federal University of Pernambuco, Cidade Universitaria, Brazil.

International Journal of Molecular Sciences, 2023 May 8;24(9):8425.
doi: 10.3390/ijms24098425.

Additional co-authors who contributed to this thesis:

Andreas Stingl and Patricia M A Farias (PHORNANO Holding GmbH) provided the zinc-oxide nanoparticles that were used for all experiments in this work.

BET-measurements were performed by Dennis Röcker (Chair of Bioseparation Engineering, TUM School of Engineering and Design, Technical University of Munich, Germany).

I would like to acknowledge the contribution of the following people to my research work:
Abuja Peter M: assistance with nanoparticle dispersion, UV/Vis spectroscopy and ROS measurements

Punz Benjamin: DLS measurement and STEM images
Rieger Julia: assistance in BSL-3 laboratory, virus neutralization assays
Dennis Röcker: BET- measurements

All co-authors have agreed to the inclusion of their published data in this work.

Funding:

This project, named ANOPSA (Antiviral NanOmaterials for Personal Safety), was funded under the Nano EHS SAFERA 2021 program by the Austrian and German federal governments in collaboration with the Austrian Research Promotion Agency (FFG) under grant agreement #888037.

Acknowledgements

In the following lines I would like to sincerely thank all the people and institution, who have supported me on my journey to this thesis.

First of all, my supervisor, Kurt Zatloukal, for his constant care and guidance during my time in his laboratory. Through him I had the opportunity to work in one of the most advanced BSL-3 laboratories in Austria and gain great experience and knowledge. The meaningful work combined with the enjoyable work environment will never let me forget the shared time. Special thanks to the entire BSL-3 team for those experiences and support as well.

My second supervisor Peter Abuja. He always took the time to answer my questions on all physical and chemical problems and regularly supported me actively in the laboratory.

My third supervisor Gregor Gorkiewicz for his constructive comments and helpful advice.

Julia Rieger, who was there to help me with all my experiments from the very beginning of the project. In addition, she performed the last experiments for me in the BSL-3 laboratory at a time when I was unable to enter the lab. I am very grateful to her for this.

Benjamin Punz for his support in the characterization of the nanoparticles and the wonderful electron microscopy images, as well as Dennis Röcker for the BET measurements. Their results greatly improved my work and gave me a better understanding of the nanoparticles.

The Doctoral School of Sustainable Health Research for the opportunity to write this thesis.

The FFG Project ANOPSA for financial support to perform the experiments.

My parents, especially my mother. Their tireless encouragement and constant reminders gave me a lot of support and strongly contributed to the completion of this work.

Table of contents

List of abbreviations

ACE2	Angiotensin-converting enzyme 2
Ag	Silver
BSA	Bovine Serum Albumin
BET	Brunauer–Emmett–Teller
BSL	Biosafety Level
CB	Conduction band
CDC	Centers for Disease Control and Prevention
CO_2	Carbon Dioxide
COVID-19	Coronavirus disease 2019
Cu	Copper
CVD	Chemical Vapor Deposition
CVD	Chemical vapor deposition
DHE	Dihydroethidium
DLS	Dynamic light scattering
DMSO	Dimethyl Sulfoxide
DVV	German Association for the Control of Virus Diseases
EDTA	Ethylenediaminetetraacetic Acid
EDX	Energy dispersive X-ray
EELS	Electron energy loss spectra
EtOH	Ethanol
FCS	Fetal Calf Serum
HEPA	high efficiency particulate air
H_2DCFDA	2',7'-Dichlorodihydrofluorescein Diacetate
H_2O_2	Hydrogen Peroxide
Hz	Hertz
IHC	Immunohistochemistry
MEM	Minimal Essential Medium
MOI	Multiplicity of Infection
N	Nucleocapsid
NP	Nanoparticle

•O2-	Superoxide radicals
•OH	Hydroxyl radical
ORF	Open reading frame
PCS	Photon Correlation Spectroscopy
PBS	Phosphate-Buffered Saline
PDI	Polydispersity Index
PenStrep	Penicillin-Streptomycin
RADAR	Radio detection and ranging
RH	Relative humidity
qRT-PCR	Quantitative Reverse Transcription Polymerase Chain Reaction
RKI	Robert Koch Institute
RdRp	RNA-dependent RNA Polymerase
ROS	Reactive Oxygen Species
S	Spike
SARS-CoV-2	Severe acute respiratory syndrome coronavirus 2
SD	Standard deviation
SEM	Scanning Electron Microscopy
STEM	Scanning Transmission Electron Microscopy
TEM	Transmission Electron Microscopy
TiO_2	Titanium dioxide
UV	Ultraviolet
UV-Vis	Ultraviolet-visible spectroscopy
VB	Valence band
VI	Virus input
VOC	Variants of concern
VOI	Variants of interest
WHO	World Health Organization
ZnO	Zinc oxide
ZnO-NP	Zinc oxide nanoparticle

List of figures

Abstract

The rapid transmission of the new severe acute respiratory syndrome coronavirus type 2 (SARS-CoV-2) during the COVID-19 pandemic, through respiratory droplets, aerosols and contaminated surfaces highlighted the need for efficient and safe inactivation as well as decontamination methods for personal protective equipment (PPE) and surfaces. Conventional approaches, such as ultraviolet radiation, heat, and liquid chemical treatments, can either damage materials or lack comprehensive disinfection efficacy. Consequently, material-friendly and sustainable alternatives are demanded. The use of nanomaterials is a promising approach since their antiviral properties are well-established. In this study, two novel zinc oxide nanoparticles (NP) (ZnO-NP-45 and ZnO-NP-76) were investigated for their antiviral activity and mechanisms against the SARS-CoV-2 Delta and Omicron variants. These NPs are of great interest because of their environmentally friendly and efficient synthesis process. Virus neutralization assays in cell-culture using human lung epithelial cells (Calu-3) showed that ZnO-NP-45 exhibited a strong virus inactivation by a factor of 10^6 at a concentration of 20 mg/mL for both virus variants. In contrast, ZnO-NP-76, demonstrated inconsistent antiviral effects with the Delta and Omicron variant. To investigate the mechanisms behind these differences in antiviral activity, the particles were characterized by their size distribution and surface charge. ZnO-NP-45 was found to be polydisperse, with particles ranging from 30 nm to 60 nm, while ZnO-NP-76 was less polydisperse, with particles ranging from 60 to 92 nm. To further investigate the antiviral mechanisms of the NPs, their production of reactive oxygen species (ROS) was investigated in vitro, both in the dark and under constant light exposure at 4200 lux. Exposure to light led to increased hydrogen peroxide levels, especially for ZnO-NP-45, while the other NPs showed no significant increase in ROS production. This observed effect could contribute to the inactivation of viruses, which makes it particularly interesting for applications such as surface coatings. The findings of this study demonstrate strong antiviral activity of ZnO-NPs against SARS-CoV-2, positioning them as potential antiviral agents. Possible applications of ZnO-NP include the antiviral coating of filters or PPE to improve the protection of users in the healthcare sector as well as in public settings.

Zusammenfassung

Die durch Tröpfcheninfektion, Aerosole und kontaminierte Oberflächen erfolgende, rasche Übertragung des Coronavirus SARS-CoV-2 (severe acute respiratory syndrome coronavirus type 2) hat während der COVID-19-Pandemie die Notwendigkeit effizienter und sicherer Dekontaminationsmethoden für persönliche Schutzausrüstung (PSA) und Oberflächen verdeutlicht. Herkömmliche Methoden wie ultraviolette Strahlung, Hitze und flüssige Chemikalien, können Materialien beschädigen oder bieten keine umfassende Desinfektion. Materialfreundliche und nachhaltige Alternativen sind daher gefragt. Nanomaterialien bieten einen vielversprechenden Ansatz, da ihre antiviralen Eigenschaften bereits gut etabliert sind. In dieser Studie wurde die antivirale Aktivität und die zugrunde liegenden Mechanismen der Zinkoxid-Nanopartikel (ZnO-NP-45 und ZnO-NP-76) gegen die SARS-CoV-2-Varianten Delta und Omikron untersucht. Diese Nanopartikel sind aufgrund ihres umweltfreundlichen und effizienten Syntheseprozesses von besonderem Interesse. Virusneutralisationstest in Zellkultur mit menschlicher Lungenepithelzellen (Calu-3) zeigten, dass ZnO-NP-45 in einer Konzentration von 20 mg/ml eine starke Inaktivierung (Faktor 10^6) für beide Virusvarianten erreichte, während ZnO-NP-76 eine nicht einheitliche antivirale Wirkung zeigte. Um die Gründe für diese unterschiedliche Aktivität zu untersuchen, wurden die Partikel hinsichtlich ihrer Größenverteilung und Oberflächenladung charakterisiert. ZnO-NP-45 erwies sich als polydispers, mit Partikeln zwischen 30 bis 60 nm, während ZnO-NP-76, mit Partikeln zwischen 60 und 92 nm, weniger polydispers war. Zur weiteren Untersuchung der antiviralen Mechanismen wurde die Produktion von reaktiven Sauerstoffspezies (ROS) in vitro sowohl im Dunkeln als auch unter konstanter Belichtung bei 4200 Lux gemessen. Die Belichtung führte insbesondere bei ZnO-NP-45 zu einer erhöhten Produktion von Wasserstoffperoxid, wogegen bei den anderen Nanopartikel kein signifikanter Anstieg der ROS-Produktion gezeigt werden konnte. Die erhöhte ROS-Produktion könnte zur Virusinaktivierung beitragen, was ZnO-NP-45 für antivirale Oberflächenbeschichtungen besonders geeignet erscheinen lässt. Die Ergebnisse dieser Studie zeigen, dass Zinkoxid-Nanopartikel, insbesondere ZnO-NP-45, eine starke antivirale Aktivität gegen SARS-CoV-2 aufweisen. Damit positionieren sie sich unter anderem als potenzielle Wirkstoffe für die Anwendung als antivirale Beschichtung von Filtern oder PSA, um den Schutz der Nutzer im Gesundheitswesen sowie in öffentlichen Bereichen zu verbessern.

1. Introduction

1.1.SARS-CoV-2

1.1.1. SARS-CoV-2 and COVID-19

The causative agent of COVID-19 (Coronavirus disease 2019), SARS-CoV-2 (severe acute respiratory syndrome coronavirus 2), emerged in December 2019 in Hubei province, China, particularly among people who had visited the Huanan Seafood Market in Wuhan (1). Since then, the virus has rapidly spread globally, reaching Austria on February 25, 2020, with a fast increase at the beginning of March 2020 (2). The World Health Organization (WHO) announced a name for the new disease on 11 February 2020: COVID-19 (3). One month later, on March 11, 2020, Dr. Tedros Adhanom Ghebreyesus, the WHO Director General, declared the outbreak a pandemic. Within five days of this declaration, the virus had caused 167,511 cases across more than 140 countries and territories, resulting in 6,606 deaths (4). From this point on, cases escalated globally. To date, the WHO has confirmed 775,552,205 cases globally and 7,050,201 deaths (last update 26 May 2024) (5). In May 2023 the WHO declared the end of COVID-19 as a public health emergency of international concern (6).

1.1.2. SARS-CoV-2 characteristics

SARS-CoV-2 is member of the family of *Coronaviridae*, which are enveloped, positive-sense single-stranded RNA viruses. Specifically, SARS-CoV-2 is classified under the *β-coronavirus* genus, group 2 (7). Its genome shares approximately 80% sequence identity with SARS-CoV (Severe Acute Respiratory Syndrome Coronavirus) and around 50% with MERS-CoV (Middle East Respiratory Syndrome Coronavirus). SARS-CoV-2 is a spherical enveloped virus and has a diameter of about 70-110 nm (8). Its genome has a size of about 30 kb and consists of a non-segmented, positive-sense, single-stranded RNA (9, 10). It features a 5′-cap structure and a 3′-poly-A tail (10). The genome includes 14 open reading frames (ORFs), with two-thirds encoding 16 nonstructural proteins (NSPs) (7). The NSPs include key enzymes and factors such as RNA-dependent RNA polymerase (RdRp), RNA binding proteins, proteases, helicase, exonuclease, and methyltransferases. NSPs are essential for viral replication, translation, and

assembly, as well as for modulating transcription, helicase activity, and the antiviral response, contributing to the virus's pathogenicity (11).

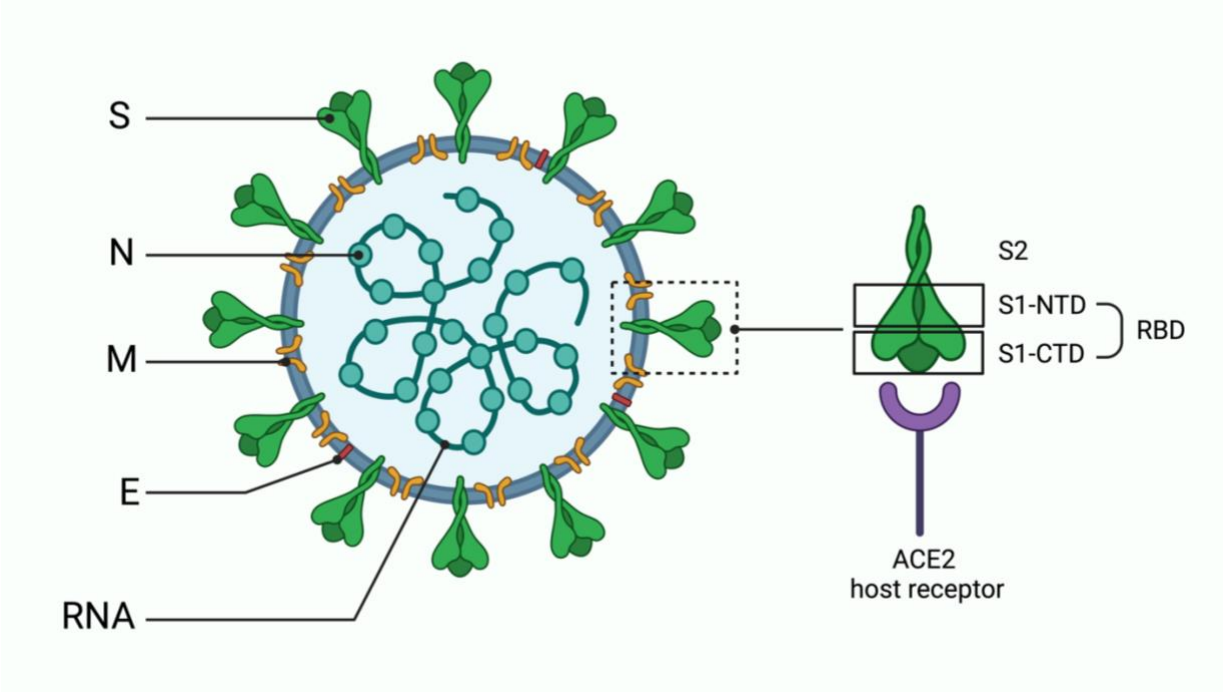

Figure 1 The Structure of coronavirus.
Illustrated are the arrangement of spike (S), membrane (M) and envelope (E) proteins. The viral RNA is bound to the nucleocapsid protein (N). ACE: angiotensin converting enzyme, RBD: receptor-binding domain, S1-NTD: N-terminal domain of spike protein, S1-CTD: C-terminal domain of spike protein, S1: amino termini of spike protein, S2: carboxy termini of spike protein. Created with Biorender.

The remaining ORFs encode nine accessory proteins along with the four structural proteins spike (S), envelope (E), membrane (M), and nucleocapsid (N) (12).

The S protein, a trimeric glycoprotein, forms a crown-like structure, giving this type of virus its name, "corona." This protein facilitates viral entry by binding to the angiotensin-converting enzyme 2 (ACE2) on the surface of host cells. The spikes are covered in polysaccharides that help to hide the virus from the host's immune system. In addition, the spike protein also determines the viral host spectrum, tissue tropism and the immune response of the host (13).

The N protein has an RNA-binding domain approximately 140 amino acids long in its core, facilitating its attachment to viral RNA. These structural proteins are linked to the viral envelope and play a crucial role in the assembly of the virus (14).

The membrane-bound (M) protein, a highly conserved transmembrane glycoprotein across *β-coronaviruses,* plays a critical role in virus assembly, RNA packaging, and virus-host interactions (14).

The small E protein, consisting of 75 amino acids, plays a crucial role in virus assembly, virion release, and morphogenesis (13). In addition to the proteins mentioned earlier, SARS-CoV-2 also produces eight accessory proteins from accessory ORFs 3a, 3b, 6, 7a, 7b, 8, 9b, and 10, which are distributed across the structural genes (13).

1.2. COVID-19 symptoms and disease

SARS-CoV-2 spreads mainly through respiratory droplets and aerosols during direct person-to-person contact (1). In addition, the virus can also spread via contaminated surfaces such as cell phones, computer keyboards or door handles due to its high stability and even fecal-oral transmission has been reported (7, 15-18). After infection with the highly contagious SARS-CoV-2 virus a variety of symptoms can occur. The incubation period is around 5 days until COVID-19 symptoms appear (19). Some individuals remain asymptomatic, while others develop mild or severe disease for 11.5 days on average (20). Infections with SARS-CoV-2 can also lead to serious illnesses such as, shortness of breath, pneumonia, kidney failure, liver failure, cardiovascular damage, cardiac arrhythmia and eventually death, especially in patients with underlying diseases (21).

Early symptoms like coughing and severe pneumonia indicate respiratory transmission, with the virus replicating in both upper and lower respiratory tracts (7). Almost 40% of patients suffer from gastrointestinal symptoms such as diarrhea and vomiting. Up to 10% of those patients show no fever or respiratory tract infections (22). Extrapulmonary manifestations include neurological symptoms such as fatigue, dizziness, and impaired consciousness; ischemic and hemorrhagic strokes; muscle damage; and eye and skin conditions (22). The disease can have long-term effects such as myocardial inflammation. Severe cases are not limited to the elderly; children and young adults are also at risk (7).

Chronic conditions that manifest after acute COVID-19, also known as long COVID, have become an increasingly important topic during the pandemic. It is characterized by symptoms lasting for months to years such as chronic fatigue, persistent shortness of breath, joint or muscle pain, memory problems, sleep disturbances, or persisting loss of taste and smell (23, 24).

Strategies to combat the virus encompass minimizing exposure, administering vaccines, and developing and testing new or existing drugs that lower the virus's infectivity. To interact with viruses and impede their replication cycle, various methods can be employed.
Blocking the initial attachment of viral proteins to host cell receptors is crucial in preventing infection (25, 26). Inhibiting viral enzymes involved in nucleic acid synthesis can disrupt the replication process(27). In addition, targeting the formation and release of new virions is crucial to stop the spread of the virus (28, 29).

1.3.SARS-CoV-2 variants

During the pandemic several variants of the SARS-CoV-2 virus have been observed and documented. The WHO introduced a nomenclature system to categorize variants into groups using Greek letters. The first reason for this approach was to facilitate communication, as Greek letters are easier to pronounce and less prone to confusion than scientific names, which consist of letters and numbers. The second reason was to avoid naming virus variants after the country of first discovery in order to prevent possible discrimination and stigmatization (30, 31). This classification also helps in distinguishing between different variants of concern (VOC) and interest (VOI) based on their impact on global public health (32). Based on this new nomenclature the first documented variant from Wuhan was named wild-type (33).
SARS-CoV-2 VOIs, for example Lambda or Mu, are specific strains of the virus that exhibit genetic changes potentially affecting virus characteristics such as transmissibility, disease severity, host immune escape, diagnostic or therapeutic resistance, or other epidemiological impacts. These variants were closely monitored by health organizations to assess their potential threat to public health (34, 35).
SARS-CoV-2 VOCs include Alpha, Beta, Gamma, Delta and Omicron.

The Alpha (B.1.1.7) variant, also known as UK or Kent variant, was first detected in England in September 2020 (36) and quickly became the dominant strain in the UK. It is characterized by multiple spike protein mutations and deletions such as Δ69/Δ70, ΔY144, N501Y, A570D, P681 h, T716I, S982A and D1118H and other genomic mutations (34). The variant has raised significant concern due to its increased transmissibility and impact on disease severity.

Infection with this variant is linked to a higher risk of hospitalization, particularly among inpatients, and increased case-fatality rates, with effects varying across different age groups (37, 38). Patients infected with the Alpha variant experience more severe clinical disease, higher viral loads, and a greater risk of death or transfer to the intensive care unit compared to other virus variants. Additionally, the Alpha variant poses a higher risk of hospitalization and mortality than the wild-type virus (39, 40).

The Beta variant, also known as B.1.351 emerged independently and rapidly spread globally. The variant was first identified in South Africa (41) and is characterized by eight mutations in the spike protein, particularly N501Y, E484K and K417N, which increase its affinity to the ACE2 receptor, enhancing infectivity (42). The Beta variant was found to have increased transmissibility in comparison to the wild-type strain and demonstrated immune escape properties (43).

The Gamma variant (P.1), or Brazilian variant, was first reported in Brazil in late 2020 (44). It rapidly became the predominant variant in Brazil and several other cities in South America. In comparison to the original Wuhan strain this variant has twelve mutations in the spike protein, such as N501Y, K417T and E484K (45). The P.1 variant is 1.7 to 2.4 times more transmissible than earlier variants and poses an increased risk of reinfection, indicating its ability to evade the immune response acquired from previous infections. In addition, an infection with the Gamma variant is 1.2 to 1.9 times more likely to result in mortality compared with previous lineages (34, 43).

The Delta variant (B.1.617.2) was first identified in the Indian city of Maharashtra in October 2020 (46). It was reported to have the highest transmissibility compared to the Alpha, Beta and Gamma variants (34). Infected individuals have a viral load approximately 1000 times greater than those infected with the wild-type strain, coupled with a higher replication rate. This explains the Delta variant's high transmissibility and why it became the dominant variant worldwide until the emergence of the Omicron variant. The Delta variant contains a mutation in the spike protein (D614G) that enhances its affinity for ACE2 receptors. Infections with this variant have been associated with increased disease severity and a higher risk of hospitalization (34, 43).

The Omicron variant (B.1.1.529) was first identified in South Africa in November 2021 (47). This variant features deletions like 69–70del, affecting detection by RT-PCR tests, and over 30 mutations in its spike protein, including around 15 in the receptor binding domain (RBD). These mutations overlap with those found in other variants of concern (VOCs), such as K417, E484, and N501. These changes are associated with enhanced transmissibility by boosting spike protein affinity for ACE2, facilitate immune evasion, and reduce neutralization by vaccine-induced antibodies (34). Infections with the Omicron variant have been associated with less severe disease and milder symptoms compared to other variants (43).

1.4.Stability and inactivation of SARS-CoV-2

Viruses are unable to replicate without a suitable host cell, but they can often survive on various surfaces for long periods of time. The SARS-CoV-2 virus has a high and long-lasting stability and can remain infectious for up to 28 days if the environmental conditions are suitable. This was demonstrated on non-porous surfaces such as glass or metal at 20 degrees and 50% relative humidity (48). Another study showed, that SARS-CoV-2 could be recovered from plastic surfaces for up to 28 days at room temperature and 40-50% relative humidity (49). Even the recovery of infectious SARS-CoV-2 for the outer layer of surgical masks was observed after 7 days (50). This high stability combined with the high contagiousness facilitated the global spread and quickly turned the outbreak into a pandemic (1).

To minimize the transmission of infectious SARS-CoV-2 not only the use of antiviral drugs, but also the disinfection and decontamination of surfaces is crucial. Ultraviolet (UV) irradiation, vaporized hydrogen peroxide, moist heat, microwave-generated steam and liquid chemicals are all known to sterilize PPE and surfaces. However, each method has its disadvantages, e.g. material damage or incomplete disinfection, as is the case with UV irradiation, which is ineffective on light-protected surfaces (51, 52). Alternatives are more material-friendly methods, such as coatings made of nanomaterials or the use of ozone (54).

There are basically two methods for decontaminating a surface, namely sterilization and disinfection:

Sterilization is the elimination of all living microorganisms on a surface, including bacterial, viruses, fungi and endospores. It is used for all items that must be completely free of any microorganisms, like surgical instruments or laboratory equipment. Effective sterilization must achieve reduction of all microbial populations by log 6 (53). Sterilization methods include the use of heat, hydrogen peroxide gas, chlorine dioxide gas, plasma, ozone and radiation (54, 55). Disinfection eliminates or reduces microbial contamination but is less effective than sterilization. According to the Robert Koch Institute (RKI) and the guidelines established by the German Association for the Control of Virus Diseases (DVV), virus-inactivating disinfectants must achieve a reduction of at least log 4 to be considered effective (56). It removes pathogenic microorganisms but does not necessarily include all microbial forms such as bacterial spores. Disinfection can be achieved at different levels as defined by the CDC, including high-level, intermediate-level and low-level disinfectants. High level-disinfection is almost equivalent to sterilization, but does not kill high numbers of bacterial spores. It is required for medical devices such as endoscopes that come into contact with mucous membranes or non-intact skin. The intermediate-level disinfection is used for non-critical medical devices such as blood pressure cuffs or stethoscopes and can eliminate most microorganisms, but does not necessarily kill bacterial spores. Low-level disinfection is used for routine cleaning of surfaces with a very low risk for transmission, such as examination tables (57). Disinfection methods include the use of chemical disinfectants such as glutaraldehyde and alcohol as well as physical methods such as ultraviolet (UV) irradiation (55, 57).

The inactivation of viruses depends on whether they are enveloped or non-enveloped. There are two different types of viruses based on their structure: enveloped viruses and non-enveloped viruses (58).

Enveloped viruses, such as herpes simplex virus, influenza or corona virus, are wrapped in a lipid bilayer that was acquired from the infected host cell during virus assembly and budding (59). This envelop makes them more susceptible to disinfectants in general. Receptors and other proteins used for the attachment to potential host cells are located on the envelope of the virus. After the loss of these receptors through chemical or physical treatments such as lipophilic disinfectants, heat or UV light the viruses lose their infectivity as they can no longer attach to their host cells (60).

Non-enveloped viruses such as norovirus or parvovirus only consist of their genetic material (DNA or RNA) enclosed within a protein capsid. Inactivation often requires denaturation of the viral capsid proteins or essential replicative proteins (61). Disinfectants that damage proteins, such as glutaraldehyde or sodium hypochlorite, may be effective at inactivating non-enveloped viruses (62). Viruses such as polio are able to maintain their infectivity through RNA alone, so disinfectants may also need to penetrate the capsid to destroy the nucleic acids (62).

The enveloped influenza A virus H1 h1 can be effectively inactivated by common disinfectants like 70% ethanol, heat and ethylene oxide (63). In contrast standard disinfectants are often not insufficient in reducing the infectivity of small non-enveloped human noroviruses, making them way more challenging to inactivate (64).

2. Nanomaterials

2.1. Nanotechnology

The concept of nanotechnology was first introduced at Caltech by the renowned theoretical physicist Richard Feynman in 1959 and experienced rapid growth over the past decade (65).
In nanotechnology, materials are used that, due to their nanoscale size, have improved physical, chemical, and biological properties as well as special functionalities (66). Nanoparticles (NP), typically between 1 and 100 nm in size, possess unique properties such as a large surface area-to-volume ratio, improved thermal conductivity, and enhanced electrochemical reactivity. These characteristics distinguish them from their bulk counterparts and make them an important material category (66, 67). Nanomaterials are now utilized in a wide range of applications, including electronics, cosmetics, food processing, agriculture, water treatment, textile manufacturing, and pharmaceuticals (66, 68, 69).
NPs exhibit a broad range of antiviral activities, such as blocking the binding of virus particles to the surface structures of host cells, the degradation of virus particles by generating reactive oxygen species (ROS), catalytic oxidation, photothermal effects and the release of metal ions or the interaction with the structure of the viral envelope and its degradation (70-73). These properties make them attractive for use in antiviral therapies, surface coatings, use in air purifier filters, in ventilation systems and antiviral fabrics (71, 73).

Antiviral nanomaterials can be categorized into metal nanomaterials, metal oxide-based nano-photocatalysts, and non-metallic nanomaterials (73).

Metal nanoparticles like silver (Ag) and copper (Cu) possess broad-spectrum antiviral properties, making them interesting for medical and environmental applications (74-77).
These nanoparticles can interact with viruses before and after they enter host cells. They adsorb onto virus surfaces, release ions to inactivate viral components, and ROS to damage viral structures. For instance, nano-Ag can directly interact with viruses, blocking transcription (78). Incorporating silver nanoparticles into air filters enhances their antiviral efficiency, although prolonged exposure and dust accumulation may reduce effectiveness (79). Copper

nanoparticles also exhibit broad-spectrum antiviral activity, potentially through electrostatic adsorption and ROS generation (80, 81). Metal catalysts containing silver or copper can block respiratory infection transmission by inhibiting viral replication (82). Their antiviral activity is influenced by factors such as ROS generation and the oxidation state of the metal (83, 84).

Metal oxide-based nano-photocatalysts, such as zinc (ZnO) or tin (IV) oxide (SnO_2), are typically semiconductors with an energy band gap separating the valence (VB) from the conduction band (CB). When exposed to light at an appropriate wavelength, electrons (e^-) can transition from the VB to the CB if the energy exceeds the band gap. This process leaves behind a positively charged hole (h^+) in the VB, where oxidation can occur. Hydroxyl radicals (•OH) are formed through reactions with water, and the electrons in the CB facilitate the reduction of absorbed oxygen atoms. This photocatalytic process generates superoxide radicals ($•O_2^-$) and other ROS and therefore provides broad antiviral activity (73, 85-87).

Previous studies have documented the antiviral properties of materials such as titanium dioxide (TiO_2), tungsten trioxide (WO_3), copper (II) oxide (CuO), zinc oxide (ZnO), and tin (IV) oxide (SnO_2) against both enveloped and non-enveloped viruses, including SARS-CoV-2 (88).

Nonmetallic nanomaterials offer the advantage of lower toxicity compared to many metallic materials, which are often heavy metals that can be harmful to human health and the environment (89). Among these, carbon-based nanomaterials have shown high antiviral activities. Carbon nanotubes, for instance, possess high surface area and efficient adsorption capabilities, making them effective in waterborne virus inactivation (90). Furthermore, carbon nanotubes coated air filters have demonstrated efficacy in capturing and deactivating viruses in aerosols (91).

Graphene, with its large surface area and high conductivity, presents another promising option for antiviral applications (92). Graphene-based materials have been utilized to coat surfaces, such as glass fiber air filter media, leading to significant reductions in viral concentrations (91). Graphene oxide, a derivative of graphene, exhibits broad-spectrum antiviral activity due to its sharp edges and electrostatic interaction with viruses (93). Additionally, graphene oxide can be combined with other materials, such as polymers or nanoparticles, to enhance its antiviral efficacy (94).

The polymer semiconductor g-C3N4, shows catalytic activity under visible light and has been explored for virus inactivation (95). Combining g-C3N4 with other semiconductors has resulted in enhanced photocatalytic efficiency against viruses (96). These non-metallic nanomaterials offer a safer and potentially more effective alternative for antiviral applications across various domains, from water treatment to air purification.

2.1.1. Synthesis of nanomaterials

In principle there are two main approaches used for the synthesis of nanomaterials, the top-down and bottom-up approaches. Top-down methods reduce the size of a bulk material toward the nanoscale, while bottom-up approaches forms nanostructures from smaller clusters and atoms, as shown in Figure 2 (97, 98).

Top-down approaches

While these methods are straightforward and relatively easy to implement, they are often less effective for producing irregularly shaped and extremely small particles. The main disadvantages of these methods are the difficulty in precisely controlling the particle size and shape, as well as the risk of impurities that can affect the properties of the nanoparticles. Examples for top-down approaches include mechanical milling, electrospinning, lithography, sputtering, arc discharge and laser ablation (97, 98).

Bottom-up approaches

Bottom-up approaches, also known as constructive technique, are the opposite of the top-down methods. Nanoparticles are formed through the growth and self-assembly of atoms and molecules, serving as building blocks. This method is very effective for producing nanoparticles with well-defined shapes, sizes, and chemical compositions. However, these methods can sometimes be more complex and time-consuming, often requiring careful control of the synthesis conditions to ensure the desired outcomes. Bottom-up approaches in nanoparticle synthesis include methods such as chemical vapor deposition (CVD), hydrothermal methods, sol-gel method and co-precipitation method (97, 98).

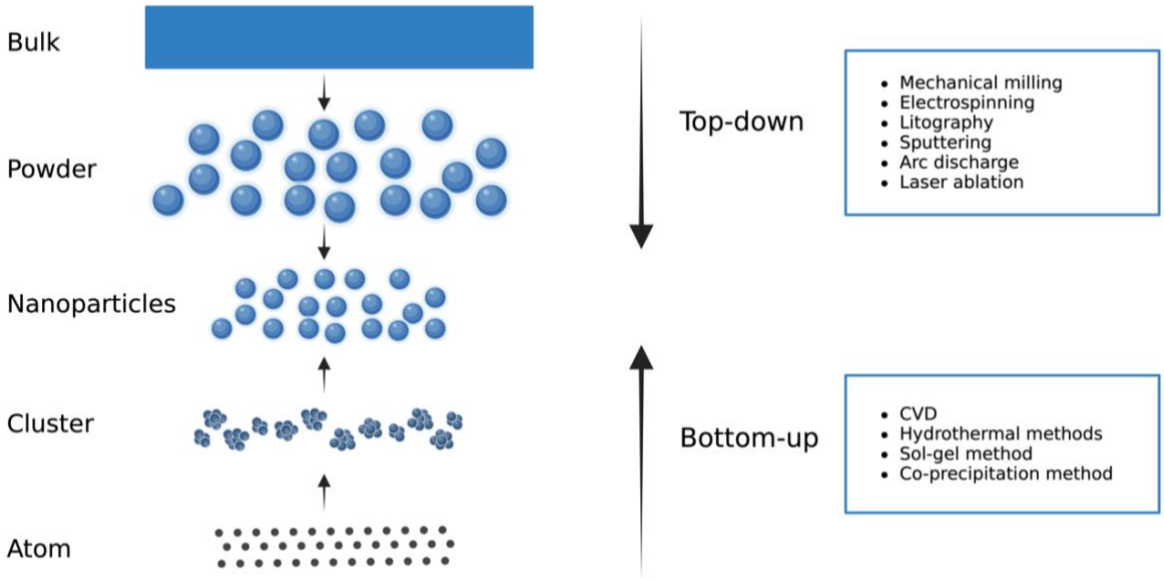

Figure 2 Principle of nanoparticle synthesis using top-down and bottom-up approaches.
Created with Biorender.

2.2. Bioanalytical methods for the characterization of NPs

Accurate characterization of nanoparticles is essential for understanding their unique properties compared to bulk materials and ensuring reliable experimental data. The two most commonly analyzed factors are the surface charge and particle size as they are responsible for a range of biological effects like toxicity and solubility dissolution (99). Popular, non-invasive and simple options for proper characterization are dynamic light scattering (DLS), zeta potential (ζ) measurements and Ultraviolet-visible spectroscopy (UV-Vis). In addition, electron microscopy is used to visualize the NPs and obtain information about their size, shape and state of aggregation.

2.2.1. Dynamic light scattering

Dynamic light scattering (DLS), also known as PCS (Photon Correlation Spectroscopy) evolved from the optical frequency advancements of post-World War II RADAR (radio

detection and ranging) technology. Unlike radio frequency RADAR, which focused on detecting individual objects' positions and velocities, DLS analyzes the diffusion of nano- and microscopic particles using optical frequencies (100, 101).

Light, usually from a laser beam, is directed at small particles in suspension. As the light hits the particles, it is scattered in all directions and is detected at a specific angle θ. The detector measures the intensity of the scattered light over time (101). Due to Brownian motion, the particles move randomly, causing fluctuations in the scattered light intensity. The Brownian motion is defined as the random movement of particles in a liquid due to bombardment by the surrounding molecules. The relationship between the size of a particle and its speed resulting from Brownian motion is defined by the Stokes-Einstein equation (100).

The time auto-correlation of the scattered light intensity reveals information about particle diffusion. The detector records these fluctuations and uses time auto-correlation to analyze the data. This involves comparing the intensity of scattered light at different times to determine how quickly the particles are moving. The rate at which the intensity fluctuates is related to the diffusion coefficient of the particles. Faster fluctuations indicate smaller particles moving quickly, while slower fluctuations indicate larger particles moving slowly. Using the diffusion coefficients, the size of the particles can be calculated through the Stokes-Einstein equation, which relates the diffusion coefficient to particle size. For samples with monodisperse particles, DLS can be used to determine a single diffusion coefficient and thus a single particle size, while polydisperse solutions provide an average diffusion coefficient (100-102).

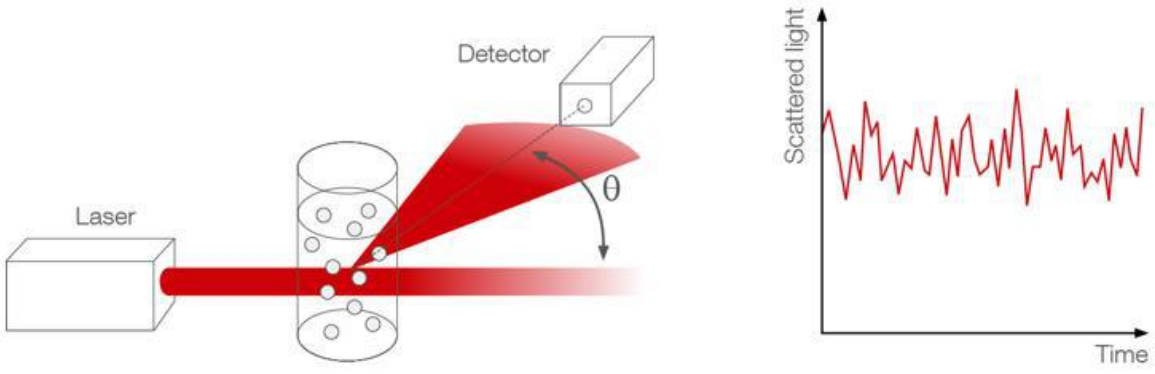

Figure 3 Basic setup of a DLS measurement system.
The functional principle of DLS is that laser light is directed onto particles in suspension. A detector with high time resolution measures the intensity of the scattered light at a specific angle θ. The intensity of the scattered light fluctuates over time due to the Brownian motion of the particles. Reproduced from (103) with permission from Anton Paar GmbH.

The technique is used for various applications in scientific and industrial sectors, where it is essential to estimate the distribution of particles in suspension as well as their size and behavior. Commonly determined parameters are hydrodynamic radius, zeta potential, polydispersity and the concentrations of nanoparticles, polymers and cells. For this reason, DLS is essential for drug development, cosmetics, and food industry product quality control (104, 105).

2.2.2. Zeta Potential

The zeta potential (ζ) is a physical property of all solid-liquid and liquid-liquid colloidal systems and is defined as the electrical potential developed at the solid-liquid interface (102, 106, 107). The surfaces of dispersed particles are surrounded by a thin layer of ions that have the opposite charge as the particle surface, the so-called Stern layer. Beyond this layer is a diffuse electric double layer, which contains ions of opposite charge moving with the particle that are loosely associated with the surface. The zeta potential is the voltage at the edge of the slipping or shear plane in relation to the dispersing medium, where ions, molecules and other substances are no longer connected to the surface of a particle. If two adjacent particles have sufficiently high zeta potentials with the same sign, they will not agglomerate due to the repulsive electrostatic forces between particles with the same charges. Alternatively, steric hindrances can be used to stabilize the particles, such as artificially produced ligands or surface groups. These can prevent the particles from agglomerating. However, such surface coatings can negatively change the properties of the particles. Therefore, the zeta potential is often an important mechanism to achieve the stability of nanoparticles in an aqueous environment. The zeta potential can be used to predict the stability of nanoparticle suspensions. Nanoparticles with a higher zeta potential than ±60 mV are considered stable. In contrast, particles with values between -10 mV and +10 mV agglomerate quickly if they are not protected by surface coatings. The zeta potential is affected by the pH value of the suspension (100, 107).

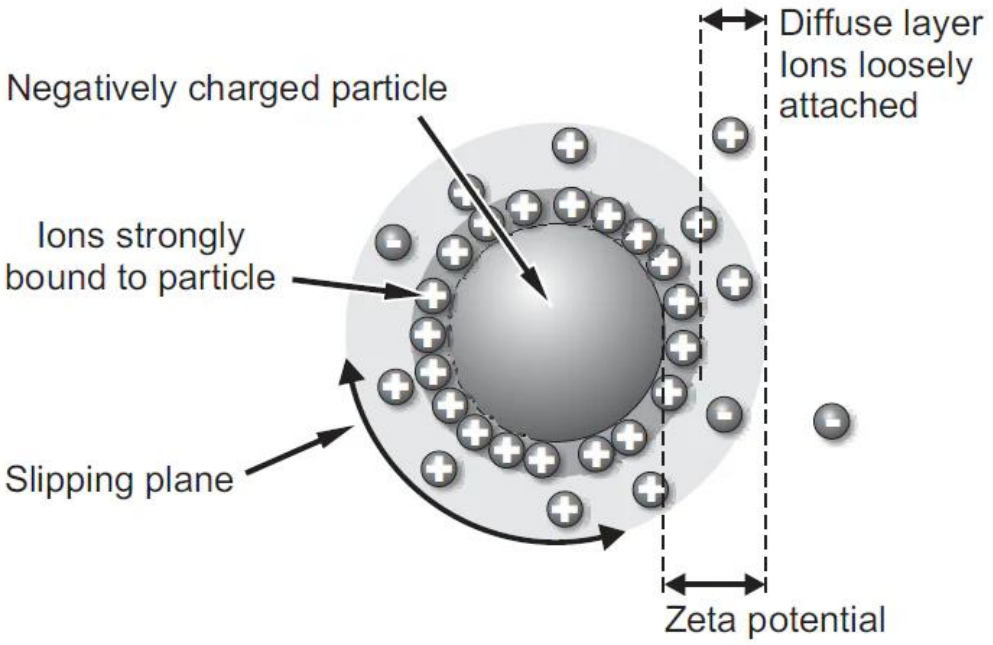

Figure 4 Schematic representation of a particle and its surrounding layers in aqueous medium.
The potential at the slipping plane is called the zeta potential. Reproduced from www.nanoComposix.com (107) with permission from Fortis Life Sciences.

2.2.3. Ultraviolet-visible spectroscopy (UV-Vis)

UV-Vis spectroscopy is a simple, fast, and reliable technique for characterizing nanoparticles. It measures the absorption, reflectance, and transmission of light in the ultraviolet (200–400 nm) and visible (400–800 nm) regions of the electromagnetic spectrum. Depending on their size, shape, and composition, nanoparticles absorb light at certain wavelengths. This absorption is directly proportional to the concentration of the nanoparticles and the path length of the sample, as described by the Beer-Lambert law:

$$A = log\left[\frac{I_0}{I}\right] = \varepsilon CL$$

Where "A" is absorbance, "I_o" is the intensity of incident light over sample cell, "I" is passing incident light through the sample cell, "ε" is the molar absorptivity constant, "C" is molar concentration and "L" is path length.

Measurements can be done using light in the wavelength of 200-800 nm. Wavelengths below 200 nm are generally not used because oxygen in the sample absorbs light in this range.

In this technique, a beam of light passes through the sample, whereby atoms and molecules absorb electromagnetic radiation at certain wavelengths due to their structure and chemical bonds. The electrons in the atoms or molecules can be excited from lower to higher energy levels when this radiation is absorbed. The resulting absorption spectrum, in which the absorption is plotted against the wavelength, provides information about the electronic structure of the sample and can be used to analyze characteristics such as the size, shape and concentration of nanoparticles (108, 109).

For amorphous semiconductors, UV-Vis spectroscopy can estimate the band gap energy between the valence band and the conduction band using the method proposed by Tauc in 1966 (110). The band gap energy describes the energy needed to excite an electron from the valence band to the conduction band (85). The optical band gap can be determined using the Tauc equation:

$$(\alpha h\nu)^{\frac{1}{\gamma}} = B(h\nu - E_g)$$

where h is the Planck constant, ν is the photon's frequency, E_g is the band gap energy, and B is a constant. The factor γ depends on the type of the electron transition and is equal to 2 for direct transition band gaps or ½ for indirect transition band gaps. By extrapolating the linear regions of the resulting plots to the abscissa, the band gap energy can be determined (110, 111). When electrons move from the valence band to the conduction band, they create empty spaces or "holes" in the valence band. In aqueous environments, these electrons and holes can interact with oxygen and hydroxyl ions, respectively, leading to the formation of reactive oxygen species (ROS), such as superoxide anion radicals and hydroxyl radicals (112). ROS are highly reactive molecules formed as byproducts of the reduction of molecular oxygen (113) and were reported to destroy proteins, lipids, carbohydrates and nucleic acids, ultimately leading to viral inactivation (114). They include species with unpaired electrons such as hydroxyl radicals ($HO^{\bullet}$), superoxide ($O_2^{\bullet-}$) and singlet oxygen ($^1O_2$) and non-radicals such as hydrogen peroxide (H_2O_2) that do not have unpaired electrons. ROS are highly reactive towards organic and inorganic species and are generated in cellular, electrochemical or metal release reactions that occur on metal-oxide NPs such as zinc oxide (113).

2.2.4. Electron microscopy

Another technique for the characterization of nanoparticles is their visualization using electron microscopy. The high resolution provides detailed information about the morphology, size, aggregation and structure of the nanoparticles. Different types of electron microscopy are used for nanoparticle characterization:

2.2.4.1. Transmission Electron Microscopy (TEM)

TEM uses a beam of electrons that is transmitted through a very thin specimen, providing a high-resolution visualization of the interior of the sample. TEM is widely used in nanomedical research to reveal fine relationships between nanoparticles and biological components. A conventional TEM can achieve a resolution of around 0.2 nm because of the very short wavelength of the electron beam.
However, biological samples require specific preparation methods such as resin embedding or cryofixation, which can have a negative impact on image quality and resolution (usually limited to ~2 nm)(115).

2.2.4.2. Scanning Electron Microscopy (SEM)

SEM uses a focused beam of electrons to scan the surface of a sample, producing images with a three-dimensional appearance. It provides high resolution (3–20 nm), making it useful for characterizing interactions between nanoparticles and cell surfaces as well as nanoparticle internalization and cell shape modifications (116).

2.2.4.3. Scanning Transmission Electron Microscopy (STEM)

STEM combines features of transmission electron microscopy (TEM) and scanning electron microscopy (SEM). Like TEM, STEM requires very thin samples and analyzes transmitted electrons, but also uses additional signals like characteristic X-rays and electron energy loss spectra (EELS) for spatially correlated analysis. STEM scans a finely focused electron beam in

a raster pattern, enabling simultaneous acquisition of multimodal data, creating a virtual image with improved spatial resolution compared to SEM.
STEM enables localized analytical data acquisition, including energy dispersive X-ray spectroscopy (EDX), oxidation state studies with EELS, and atomic resolution imaging (117).

2.2.4.4. Energy dispersive X-ray (EDX) spectroscopy

EDX microanalysis is a widely used technique to identify the elemental composition of a sample and is used together with a scanning electron microscope (SEM). The technique can quickly generate information about the chemical composition of the sample as well as the distribution and concentration of the present elements. In EDX analysis, an electron beam displaces an electron from the inner shell of an atom, creating a hole. An electron from the outer shell fills this gap and releases energy in the form of X-rays, which are typical for the element in question. A silicon drift detector captures these X-rays and the software interprets the signals for element classification and line scanning. The advantages of this method are the minimal sample preparation and the fact that it is non-destructive (118).

2.3. Zinc Oxide Nanoparticles

2.3.1. Zinc-oxide-nanoparticles and their applications

Zinc oxide (ZnO) is a versatile and promising inorganic material with a wide range of applications. As an II–VI semiconductor, ZnO has a direct wide bandgap of about 3.37 eV at room temperature and high excitation binding energy (60meV)(119, 120). ZnO-NPs are the most commonly used metal oxide nanoparticles due to their low toxicity and wide range of potential applications (121).
The US Food and Drug Administration has recognized ZnO-NPs as a generally safe and nonhemolytic substance (122). ZnO-NPs exhibit unique properties such as high catalytic and photochemical activities, as well as antibacterial, antifungal and antiviral properties (121). In addition, ZnO-NPs have high absorption in the UVA and UVB regions, which makes them

effective UV protectors in sunscreens and other cosmetic products (123). The widespread use of ZnO-NPs in biomedicine is attributed to their biocompatibility, low toxicity, ability to generate ROS and release zinc ions (124).

The antibacterial effect of ZnO-NPs is based on their ability to release zinc ions into the cells inhibiting respiratory enzymes and causing ROS formation. This damages bacterial membranes, DNA, and mitochondria, leading to cell death (125). ZnO-NPs were shown to be effective against multi-drug-resistant bacteria (126). In addition, ZnO-NPs exhibit strong antifungal activity, which is influenced by their size, morphology, dose and source of synthesis. ZnO-NPs penetrate fungal cells, disrupting mitochondrial function, generating ROS, and releasing Zn^{2+} ions, causing DNA damage and cell death (127, 128). When combined with fluconazole, ZnO-NPs have a synergistic effect against *Candida albicans*, and when combined with thiram, they synergistically inhibit *Phytophthora* growth (129, 130).

The antiviral activity of ZnO-NPs has been demonstrated for various viruses, including rhinovirus (131), human immunodeficiency virus (HIV)(132), hepatitis E and hepatitis C (133), influenza (134), herpes simplex viruses (135), human rotavirus (136) and more recently, SARS-CoV-2 (137).

2.3.2. Synthesis of ZnO-NP

Zinc oxide (ZnO) nanoparticles can be synthesized using various methods, as already described above, allowing control over their shape and size for specific applications. The synthesis method and key parameters like solvent type, precursors, pH, and temperature determine the resulting morphology and size. Common morphologies of ZnO nanostructures include nanosized rods, spheres, tubes, wires, needles and rings. Other complex shapes like nanosized belts, cages, combs and springs can also be synthesized (66).

For this study, two types of ZnO-NPs, ZnO-NP-45 and ZnO-NP-76, were synthesized using a modified green sol-gel method with whey, a dairy by-product, as an eco-friendly chelating agent instead of conventional chemicals. This new bottom-up method, was described by Soares et al. in 2020 (138).

In a first step, zinc citrate was prepared from $Zn(NO_3)_2.6H_2O$, by mixing with citric acid at a molar ratio of 1:3. To promote citrate polymerization whey was added to the solution to produce

a stable resin (xerogel). Subsequently, the xerogel was calcined at various temperatures (200°C to 1000°C) to yield ZnO-NPs. The resulting NPs were characterized using X-ray diffraction (XRD), TEM, Raman spectroscopy, and UV-visible spectroscopy.

UV-visible absorption spectroscopy showed a characteristic ZnO absorption peak at a wavelength range of 315-340 nm, with a redshift in the absorption edge as calcination temperature increased. TEM analysis revealed a spherical morphology and high agglomeration of nanoparticles, with sizes ranging from 20 to 120 nm depending on the calcination temperature. Selected area electron diffraction patterns confirmed the high crystallinity of the nanoparticles (138).

3. Aim of the study and hypothesis

The aim of this research was to investigate the antiviral activity of two zinc oxide nanoparticles, ZnO-NP-45 and ZnO-NP-76, against SARS-CoV-2 and its relevant variants using cell culture-based virus neutralization assays. In addition, both NPs were characterized using different methods to better understand their antiviral properties. These NPs are of particular interest due to their innovative, environmentally friendly and sustainable synthesis process. The findings of this study can play an important role in the development of antiviral coatings for PPE and air filters that improve user safety and help prevent the spread of pathogens such as SARS-CoV-2.

4. Material & Methods

4.1. Synthesis of ZnO-NPs

The two nanomaterials ZnO-NP-45 and ZnO-NP-76 were provided by Phornano Holding GmbH (Korneuburg, Austria). The NPs were produced using a modified green sol-gel method according to Soares et al. (2020)(138). This whey-assisted sol-gel technique effectively controlled nanocrystal growth through gel composition and calcination temperature, resulting in highly crystalline ZnO-NPs. For comparison, commercially available ZnO-NPs with a size of <100 nm (Cat # 544906, Sigma-Aldrich) were used in separate test series (139).

4.2. Preparation of ZnO-NPs

The ZnO-NPs were rinsed with 70% EtOH and left to air dry overnight. Before work, the appropriate amount of each ZnO-NP preparation was measured into 5 mL Eppendorf tubes and dispersed in Minimal Essential Medium (MEM) (Thermo Fisher Scientific, Waltham, MA, USA) medium, without fetal calf serum (FCS) (Thermo Fisher Scientific, Waltham, MA, USA), to prevent non-specific adsorption to bovine serum albumin (BSA) and other serum proteins. The suspensions were mixed for 30 seconds with a vortex mixer before each working step to reduce agglomeration and sedimentation (139).

4.3. Cell culture

For the virus neutralization assays, Calu-3 (Biomedica, Vienna, Austria), a human lung epithelial cells line derived from non-small cell lung carcinoma, were used. They were selected for this study because they originate from the human respiratory tract and are therefore a good model for SARS-CoV-2 viruses that infect the respiratory tract (140). Calu-3 cells were cultured in MEM supplemented with 10% FCS, 2% L-glutamine (Merck KGaA, Darmstadt, Germany), and 1% Penicillin-Streptomycin (PenStrep) (Thermo Fisher Scientific, Waltham, MA, USA). VeroE6 cells (Biomedica, Vienna, Austria) were used to propagate the SARS-CoV-2 virus.

These cells were obtained from the kidney of an African green monkey (*Cercopithecus aethiops)* in the 1960s (141). The VeroE6 cell line has been used extensively in virological studies and expresses the ACE2 receptor that SARS-CoV-2 uses to invade host cells (142). VeroE6 cells (Biomedica, Vienna, Austria) were grown in MEM with 5% FCS, 2% L-glutamine, and 1% PenStrep. Both cell lines were cultured at 37 °C and 5% CO_2 (139).

4.4. Metabolic interference assay

The potential metabolic interference of ZnO-NPs on Calu-3 (human lung epithelial) cells was assessed using the resazurin reduction assay. In metabolically active cells, the non-toxic dye resazurin is reduced by mitochondrial reductases to the highly fluorescent resorufin. Over a wide range of concentrations, the number of viable cells it proportional to the fluorescence output. The resorufin concentration was measured fluorometrically at an excitation wavelength of 530 nm and an emission wavelength of 590 nm (143-145). For our experiments, the optimal excitation wavelength was determined to be 485 nm.

A 1 mM stock solution of resazurin (Sigma Aldrich R7017-1G, Merck KGaA, Darmstadt, Germany) was prepared in phosphate-buffered saline (PBS) (Thermo Fisher Scientific, Waltham, MA, USA), filtered using sterile 0.2 µm syringe filters (Thermo Fisher Scientific, Waltham, MA, USA), and stored at 4 °C in the dark.

To assess potential metabolic interference, the resazurin reduction assay was performed under the same experimental conditions as the virus neutralization assays, excluding the virus.

Calu-3 cells were seeded into 48-well microtiter plates (Corning Incorporated, Kennebunk, ME, USA) at a density of 30,000 cells per well and incubated at 37 °C and 5% CO_2 for 48 h prior to the assay. ZnO-NPs suspensions were prepared in MEM medium containing 2% L-glutamine and 1% Penicillin-Streptomycin in decreasing concentrations (100, 80, 40, 20, 10, 5, and 1 mg/mL).

The ZnO-NP suspensions were incubated 1 h at 37 °C and 300 min^{-1}, then centrifuged at 13,000× g for 5 min. The supernatant was collected and applied to the cells for 1 h at 37 °C and 5% CO_2. Afterwards, the cells were washed with MEM and fresh medium containing 10% FCS, 2% L-glutamine and 1% Penicillin–Streptomycin, was added. Untreated cells served as references. The plates were incubated at 37 °C and 5% CO_2 for 48 h.

Resazurin was added to each well at a final concentration of 10 µM to measure the metabolic activity of the cells. The fluorescent signal was measured using a microplate reader (Agilent BioTek Synergy 4, Fisher Scientific, Göteborg, Sweden) at an excitation/emission wavelength of 485/590 nm over 2 h at 37 °C. Forty-eight hours after treatment with ZnO-NPs at each concentration, the metabolic activity of the cells was measured. Linear regression equations were derived from the recorded signals and the corresponding slopes were normalized to the reference value and plotted on a graph (139).

4.5. Working with SARS-CoV-2

SARS-CoV-2 has been classified as a risk group 3 pathogen by the WHO (146) and the European Commission (147) and requires strict biosafety protocols due to its potential to cause severe disease and its high risk of transmission. The experiments performed as a part of this project involved high concentrations of infectious SARS-CoV-2, particularly the Delta and Omicron variants. Consequently, all experiments with infectious virus were done under biosafety level 3 (BSL-3) conditions (148). These include strict access controls, special PPE, the use of HEPA (high efficiency particulate air) filters and other safety measures, all based on a comprehensive risk assessment (144).

4.6. Preparation of SARS-CoV-2 virus stocks

All experiments involving infectious virus were performed under BSL-3 containment conditions (148). The experimental series included a SARS-CoV-2 Delta virus patient isolate (isolated at the Diagnostic and Research Institute of Pathology, Graz, Austria, GISAID accession number EPI_ISL_4847176 delta-like variant) and a SARS-CoV-2 Omicron variant (Strain HCOV-19/Netherlands/NH-EMC-1720/2021, Omicron variant, Lineage B.1.1.529—Calu 3 culture, Erasmus-MC). Both variants were propagated in VeroE6 cells at 37 °C and 5% CO_2 for 72 h. To release intracellular viral particles from the adherent cells in the culture flasks, the cells were subjected to a freeze-thaw cycle, followed by centrifugation at 3000× g for 10 min to remove cell debris. The resulting supernatant was sterile filtered using 0.2 µm syringe filters (Thermo Fisher Scientific). Virus stocks were kept at −80 °C until use.

The virus titer was determined by a focus-forming assay (149). In brief, VeroE6 cells at 100% confluence were infected with 200 µL of a 10-fold serially diluted virus for 1 h at 37 °C and 5% CO_2. Following infection, the cells were washed with MEM, and 500 µL overlay medium (1.5% carboxymethylcellulose sodium salt in MEM with 2% FCS and 1% PenStrep) was applied to each well. The cells were incubated for 72 h at 37 °C and 5% CO_2. After incubation, the cells were fixed with 4% neutral-buffered formalin (SAV Liquid Production GmbH, Flintsbach am Inn, Germany) for 30 min. Antibody staining was then performed according to the following immunohistochemistry protocol to determine the number of infected cells (139).

4.7.SARS-CoV-2-neutralization assay

To evaluate the neutralizing effect of ZnO-NPs on SARS-CoV-2, Calu-3 cells were seeded into 48-well cell culture plates at a density of 30,000 cells per well, 48 h prior to the neutralization assay. Based on findings from the resazurin assay, ZnO-NP concentrations of 20, 10, and 5 mg/mL (prepared in MEM without FCS) were selected for testing. SARS-CoV-2 Delta or Omicron, depending on the experimental protocol, at a MOI (multiplicity of infection) of 0.002 was added to the prepared ZnO-NP solutions and incubated for 1 h at 37 °C and 300 min^{-1}.
Then the samples were centrifuged for 5 min at 13,000× g, and the supernatants were transferred to fresh tubes. To determine the virus input (VI) used for cell infection, 140 µL of each supernatant was collected for RNA isolation and subsequent qRT-PCR analysis (reverse transcription quantitative polymerase chain reaction). Each NP concentration was tested in five replicates by infecting five wells per supernatant tube for 1 h at 37 °C and 5% CO_2. Virus samples without NP pretreatment served as positive controls, while non-infected cells were used as negative controls. After infection, the cells were washed with MEM (without FCS), and fresh MEM supplemented with 10% FCS was added. After 48 h incubation at 37 °C and 5% CO_2, the supernatants were collected from each well to determine virus concentrations at t48 (timepoint 48 h after infection) using RNA isolation and qRT-PCR (139).

4.8. Viral RNA Isolation and Quantitative Reverse Transcription PCR (qRT-PCR)

SARS-CoV-2 RNA was extracted from cell culture supernatant using the QIAamp® Viral RNA Mini Kit (Qiagen GmbH, Hilden, Germany) following the manufacturer's instructions. The extracted RNA samples were eluted in 40 µL Milli-Q water and stored at −80 °C until further use. Viral replication was detected via qRT-PCR performed on a Rotor-Gene Q thermal cycler (Qiagen) with the QuantiTect®Probe PCR Kit (Qiagen).

The primers and probe sequences (Table 1) used in the analysis were supplied by Eurofins Genomics (Ebersberg, Germany) and were recommended by the Centers for Disease Control and Prevention (CDC) in February 2020 (26). The thermal profile is shown in Table 2.

Table 1 Primers and probe sequence

Name	Description	Sequence (5' > 3')
2019-nCoV_N2-F	Forward primer	TTA CAA ACA TTG GCC GCA AA
2019-nCoV-N2-R	Reverse primer	GCG CGA CAT TCC GAA GAA
2019-nCoV_N2-P	Probe	FAM-ACA ATT TGC CCC CAG CGC TTC AG-BHQ1

Table 2 qRT-PCR thermal profile

Step	Temperature	Time
Reverse Transcription	50°C	30 min
Initial Denaturation	95 °C	15 min
Amplification (45 cycles)	95 °C	3 s
Annealing/Extension	55 °C	30 s

Each qRT-PCR analysis was performed in a total volume of 25 µL (139).

4.9. Immunohistochemistry

For immunohistochemical staining, both SARS-CoV-2 infected and non-infected control cells were fixed in 4% neutral-buffered formalin (SAV Liquid Production GmbH, Flintsbach am Inn, Germany) for a minimum of 30 min, followed by three washes with PBS (Gatt-Koller GmbH,

Absam, Austria). The fixed cells were then treated with 0.1% Triton X-100 (Merck KGaA, Darmstadt, Germany) for 10 min and subsequently washed three times with PBS.

Next, the cells were incubated for 30 min in 3% H_2O_2 (Merck KGaA, Darmstadt, Germany) dissolved in methanol (Merck KGaA, Darmstadt, Germany) and washed again with PBS. The primary antibody specific to the SARS-CoV-2 nucleocapsid protein (Sino Biological, Beijing, China, Cat# 40143-V08B) was diluted at 1:1000 in Dako REAL™ Antibody Diluent (Dako, Glostrup, Denmark) and applied to the cells for 1 h at room temperature. Following incubation, the cells were washed three times with PBS again. The EnVision Detection Systems reagent (Peroxidase/DAB, Rabbit/Mouse, Agilent Dako, Cat# K5007) was then added and incubated for 30 min, followed by another three PBS washes. To visualize the bound secondary antibodies, DAB + Chromogen X50 (Agilent Dako, Cat# K5007) was applied to each well. The reaction was terminated by adding PBS, and the cells were rinsed with PBS to remove any residual reagent. Fresh PBS was added to maintain the cells hydrated.

Images were captured using a light microscope (Nikon, Eclipse, TS100; Nikon Europe BV, Amsterdam, The Netherlands) equipped with a JENOPTIK GRYPHAX® camera (Breitschopf, Innsbruck, Austria). SARS-CoV-2 infected cells appeared red as a result of the antibody staining (139).

4.10. Scanning transmission electron microscopy (STEM)

The primary particle size of the ZnO-NPs was analyzed by Benjamin Punz (Paris Lodron University, Salzburg, Austria) using scanning transmission electron microscopy (STEM). For this analysis, 2 µL of a 10 µg/mL NP dispersion was applied to a lacy carbon-coated copper TEM grid and dried overnight. To avoid overloading the grid, a low NP quantity (20 ng) was used to ensure the presence of single particles and small agglomerates. No additional fixation of the sample was required. Imaging was performed with a JEM F200 electron microscope (JEOL, Freising, Germany) operating in STEM mode at 200 kV. The strong contrast observed in STEM imaging results from the detection of scattered electrons.

In contrast to TEM, where parallel electron beams are focused perpendicular to the sample, STEM uses a converging electron beam that is focused at a large angle. The transmitted signal is captured as the focused beam scans the sample and provides detailed structural information.

STEM was chosen over TEM because it allows insights into the structural features of the sample that are difficult to achieve with TEM. The primary particle size was determined by calculating the mean ± standard deviation (SD) based on measurements of at least 10 particles. These measurements were performed manually using the ImageJ software (NIH, Bethesda, MD, USA) for image processing (139).

4.11. Hydrodynamic size and zeta potential of ZnO-NPs

The hydrodynamic size and zeta potential of the ZnO-NPs were assessed by Benjamin Punz using DLS. A NP concentration of 100 µg/mL was prepared in a total volume of 1 mL Millipore water. The solution was then injected into a clear disposable zeta cell (Malvern, DTS1070). Measurements were performed with the ZetaSizerNano ZS (Malvern Panalytical, Malvern, UK) using ZetaSizer Software (Malvern, 7.03, Malvern Panalytical, Malvern, UK), adjusting settings to match the refractive index of the nanoparticle composition and dispersant (2.0 for zinc oxide) (139).

4.12. Ultraviolet/visible light (UV/VIS) spectroscopy

UV/Vis spectroscopy for the three nanomaterials was performed in triplicates at a concentration of 3 mg/mL in phosphate-buffered saline (PBS) (Thermo Fisher Scientific, Waltham, MA, USA). Measurements were carried out using 100 µL per well in a 96-well UV-transparent microplate (Merck KGaA, Darmstadt, Germany) with a microplate reader (Agilent BioTek Synergy 4, Fisher Scientific, Göteborg, Sweden) at room temperature. The suspensions were scanned from 350 to 800 nm in 10 nm steps. PBS was used as a blank control and its values were subtracted from the NP readings before plotting.

4.13. Tauc plot

In 1966, Tauc proposed a method for estimating the band gap energy of amorphous semiconductors using UV/Vis spectra (110). Zinc oxide (ZnO), a II-VI compound

semiconductor, is a direct band gap semiconductor. Briefly, UV/Vis spectroscopy data were measured as described in 4.12, and the optical band gap was calculated using the Tauc equation:

$$(\alpha h\nu)^{\frac{1}{\gamma}} = B(h\nu - E_g)$$

where h is the Planck constant, ν is the photon frequency, E_g is the band gap energy, and B is a constant. The factor γ depends on the type of electron transition and is 2 for direct and ½ for indirect transitions. For ZnO, a direct band semiconductor, the factor γ is 2. The data obtained from the UV/Vis measurement were plotted in a graph. The y-axis represents $(\alpha h\nu)^2$, and the x-axis represents the photon energy $h\nu$. Linear regions of the resulting plots were extrapolated to intersect the x-axis. The point at which this line intersects the x-axis corresponds to the optical band gap energy E_g (110, 111).

4.14. ROS measurements

To estimate the ROS production of the three different nanomaterials the two fluorescent compounds dihydroethidium (DHE) (Merck, Darmstadt, Deutschland) and 2',7'-dichlorodihydrofluorescein diacetate (H_2DCFDA) (Merck, Darmstadt, Deutschland) were used. DHE, chemically reduced ethidium, serves as a redox indicator primarily for superoxide ($O_2^{\bullet -}$) and ROS with higher reactivity, showing minimal reactivity with hydrogen peroxide (H_2O_2)(150). It exhibits blue fluorescence with a maximum excitation wavelength of 370 nm and a maximum emission wavelength of 420 nm. After oxidation it shows red fluorescence with a maximum excitation wavelength of 300 nm and maximum emission wavelength of 610 nm (151).

The second redox indicator H_2DCFDA is chemically reduced fluorescein (152). It reacts with any ROS species, including H_2O_2. During oxidation by ROS the nonfluorescent dye is converted to the highly fluorescent 2',7' dichlorofluorescein (DCF) with a maximum excitation wavelength of 495 nm and a maximum emission wavelength of 527 nm (152). Both indicators are cell permeable but can also be used in solution without living cells. The quantity of produced ROS is correlated with the fluorescence intensity of the dyes and can be measured using a microplate reader. The production of ROS was measured in the dark and under constant light

exposure, as explained in detail in 4.15 and 4.16. Each condition was tested in two independent experiments, with three technical triplicates for each.

4.15. Incubation in the dark

For ROS measurement, DHE and H_2DCFDA stocks (10 mM) were prepared in DMSO (Merck KGaA, Darmstadt, Germany) and diluted in PBS to 1 mM. The stocks were stored at -20°C. Since the virus neutralization tests showed the highest inactivation rates at NP concentrations of 20 mg/ml (139), the ROS measurements were also performed at this concentration. The required amounts of ZnO-NP-45, ZnO-NP-76 and ZnO-NP-ref were weighed into 2 ml Eppendorf tubes and suspended in PBS. Either fluorescent compound was added to the NPs to reach a final concentration of 5 µM per tube in separate experiments. The suspensions were incubated in the dark for 1 h at room temperature under continuous shaking (300 min^{-1}). PBS with 5 µM of one or the other redox indicator depending on the sample was used as a control. Measurements were performed in triplicates. Following incubation, the tubes were centrifuged at 13,000x g for 5 min. Subsequently, 500 µl of the supernatant from each tube was transferred into a 24-well microplate (Corning Incorporated, Kennebunk, ME, USA). Fluorescence intensity was measured using a microplate reader.

4.16. Incubation under constant light exposure

To investigate the influence of light on ROS production, the measurements were repeated under constant light exposure using the experimental conditions described above.
The NP suspensions were incubated in a 24-well plate under constant shaking (300 min^{-1}) at room temperature and illuminated at 4200 lux using a daylight LED lamp (Lumeno, 7215GN-MKII, 10 watts, Heuchelheim, Germany). A photo of the experimental setup can be seen in Figure 5. After the incubation period the suspensions were transferred to Eppendorf tubes and centrifuged at 13,000x g for 5 min. The supernatant of each tube (500 µl) was transferred into a 24-well microplate (Corning Incorporated, Kennebunk, ME, USA). Fluorescence intensity was measured using a microplate reader.

Figure 5 Experimental setup for the measurement of ROS production under constant light exposure. The NP suspensions were incubated in a 24-well microtiter plate for 1 h at room temperature under constant shaking (300 min-1).

4.17. BET surface area determination

The specific surface area of the ZnO-NPs was determined using the Brunauer-Emmett-Teller (BET) method. This technique provides important information about the surface area of solid or porous materials by analyzing the adsorption of an inert gas (usually nitrogen) on the surface of a sample at the atomic level. Since most gases interact with solids, cooling the sample with liquid nitrogen (77 K) ensures that adsorption takes place under controlled conditions. During the analysis, the sample temperature remains constant while the pressure of the absorbing gas is gradually increased. This results in more and more gas molecules being adsorbed on the surface of the sample until the entire surface is covered with a single or monolayer. The amount of gas required to form the monolayer is measured by the absorbed volume. The accessible surface area of the material can be calculated from knowledge of the cross-sectional area of the

adsorbed gas molecules. Gas adsorption as a function of pressure does not follow a simple linear relationship, and therefore a suitable mathematical model, the BET equation, is used to calculate the specific surface area (153).

The BET equation (named after Brunauer, Emmett and Teller, who developed this theory) was first published in 1938 (154). It describes the relationship between the number of adsorbed gas molecules (X) at a given relative pressure (P/P_0), where C is a second parameter related to the heat of adsorption.

$$\frac{1}{X[(P_0/P)-1]} = \frac{1}{X_m C} + \frac{C-1}{X_m C}\left(\frac{P}{P_0}\right)$$

The BET equation describes a linear relationship between $1/[X(P_0/P)-1]$ and P/P_0, which is valid for most solids within a limited range of the adsorption isotherm (typically P/P_0 =0.05-0.35 when nitrogen is used as the adsorbate). By plotting ($1/[X(P_0/P)-1]$) against (P/P_0), the slope and intercept of the linear region can be determined, allowing X_m and C to be calculated.

The surface area (SA) is then calculated as follows:

$$SA = \frac{1}{slope + intercept} \cdot CSA$$

Where CSA is the cross-sectional area of the adsorbate (155).

The specific surface area of the ZnO-NP was determined using N_2 as adsorbate, with measurements performed at 77 K, which was achieved by cooling with liquid N_2. During the analysis, N_2 adsorption occurred over a defined pressure range and the amount of adsorbed or desorbed gas was measured. The data was plotted as an adsorption-desorption isotherm, and the linear part of the isotherm was analyzed using the BET equation to calculate the specific surface area. The measurements and calculations were performed by Dennis Röcker (TU Munich, Germany).

4.18. Data analysis

Data analysis, copy number calculations, statistical evaluations, and graphical visualizations were conducted using Dotmatics GraphPad Prism 9 (Boston, Massachusetts). Statistical differences between groups were evaluated using the Kruskal–Wallis test with correction for multiple comparisons. The significance levels were specified as follows: ns = $p > 0.05$, * = $p \leq 0.05$, ** = $p \leq 0.01$, *** = $p \leq 0.001$, and **** = $p \leq 0.0001$.

Virus copy numbers were determined using a calibration curve based on a certified RNA standard (VR-1986DTM from 2019 Novel Coronavirus, Lot: 70035624, ATCC, Glasgow, UK). This commercially available standard contained 4.73×10^3 genome copies per µL and was serially diluted for analysis via qRT-PCR (149). The cycle quantification (cq) values obtained were plotted against the natural logarithm of the copy numbers [ln(copy numbers)], and linear regression analysis was used to generate the equation for calculating copy numbers from cq values.

$$y = 1.5x + 38.4$$

This standard curve provided the relationship between cq values and virus copy numbers (139).

5. Results

5.1. Preparation of ZnO-NPs

Before starting the virus neutralization assays using the two ZnO-NPs, their behavior in suspension had to be tested. After washing with 70% EtOH and drying the NPs were suspended in MEM without FCS. It was found that the ZnO-NPs precipitate within short time and also tend to form agglomerates. Attempts to improve the stability of the suspension included the use of ultrasonic treatment, pH adjustments or alternative solvents. Neither ultrasonic homogenization nor pH changes or other solvents improved the stability of the ZnO-NP suspensions. Consequently, the samples were mixed immediately before each step to obtain the suspension as well as possible (139).

5.1.1. Metabolic interference assay

To analyze the impact of ZnO-NPs on the metabolic activity of Calu-3 cells, the resazurin reduction assay was performed to identify NP concentrations that do not cause metabolic or cytotoxicity effects. This step is of great importance, as excessive NP concentrations could impair cell function and possibly interfere with virus replication, leading to false-positive outcomes in the neutralization assays.

In order to obtain the most realistic results possible, the metabolic interference assay was conducted according to the same protocol as for the virus neutralization assays, with the exception of the addition of SARS-CoV-2. Briefly, the impact of ZnO-NP-45 and ZnO-NP-76 on the metabolic activity of Calu-3 cells was evaluated 48 h after exposure to the ZnO-NPs suspensions at increasing concentrations from 1 mg/mL to 100 mg/mL. The resulting metabolic activity was then normalized to that of untreated Calu-3 cells (Figure 6).

Both ZnO-NPs did not notably affect the viability and metabolic activity of the Calu-3 cells at concentrations of up to 20 mg/mL. However, at concentrations between 40 mg/mL and 100 mg/mL a decrease in metabolic activity was observed. At a ZnO-NP concentration of 100 mg/mL the cells retained 30-35% of their metabolic activity compared to non-treated cells (139). Consequently, ZnO-NP concentrations of 20 mg/mL, 10 mg/mL and 5 mg/mL were chosen for the virus neutralization tests.

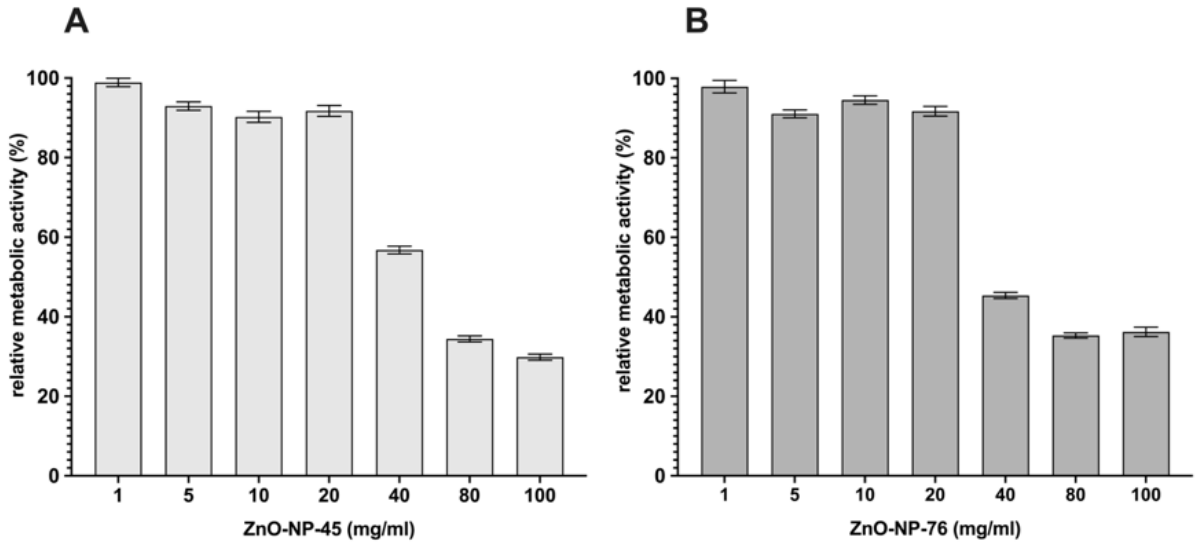

Figure 6 Metabolic interference assay of Calu-3 cells treated with ZnO-NPs.
Relative metabolic activity (%) of cells after exposure to ZnO-NP-45 (A) and ZnO-NP-76 (B) in increasing concentrations. Calu-3 cells were seeded in 48-well plates 48 h prior to the assay. The NPs were suspended in MEM, without FCS and incubated for 1 h at 37 °C under constant shaking at 300 min^{-1}. Following incubation, the suspensions were centrifuged, and the supernatant was added to Calu-3 cells for 1 h at 37 °C and 5% CO_2. After incubation the cells were washed and fresh medium containing 10% FCS was added. Metabolic activity was measured using the resazurin reduction assay after 48 h incubation at 37 °C and 5% CO_2. The bars represent the relative metabolic activity of the cells (%) normalized to that of untreated control cells. Source: Wolfgruber et. al, 2023 (139).

5.2. Antiviral activity of ZnO-NPs on SARS-CoV-2 Delta

5.2.1. ZnO-NP-45

Pre-incubation of the Delta variant with ZnO-NP-45 at concentrations of 20 mg/mL, 10 mg/mL and 5 mg/mL led to a dose-dependent decrease in the number of viral copies present in the supernatant after centrifugation (VI), compared to the untreated positive control (pos Ctrl). This reduction, summarized in Figure 7A from three independent experiments, is likely due to the adsorption of viruses to the NP surfaces, followed by their removal during centrifugation and precipitation (139).

It is crucial to note that although the viral copy number in the supernatant (VI) can be quantified, infectivity remains unknown and therefore further testing is required. To evaluate the infectivity of the remaining virus particles, the supernatant was used to infect Calu-3 cells. Forty-eight hours post infection, the virus concentration in the cell culture supernatant was determined by qRT-PCR to analyze viral replication (Figure 7B). Following treatment with 20 mg/mL ZnO-NP-45, the virus copy numbers in the supernatant of infected cells were reduced by over a factor of 10^6 across all samples, compared to cells infected with the untreated virus (pos Ctrl) (139). Pretreatment using 10 mg/mL ZnO-NP-45 also showed a trend toward reduced viral replication, although this was not consistent across all samples. At 5 mg/mL ZnO-NP-45, individual experimental replicates showed greater variability, ranging from strong virus neutralization in some samples to high replication levels comparable to the positive control (139). The observed virus inactivation at 20 mg/mL ZnO-NP-45 cannot be fully explained by the loss of virus particles during centrifugation and precipitation, but may involve other antiviral mechanisms triggered by the ZnO-NPs.

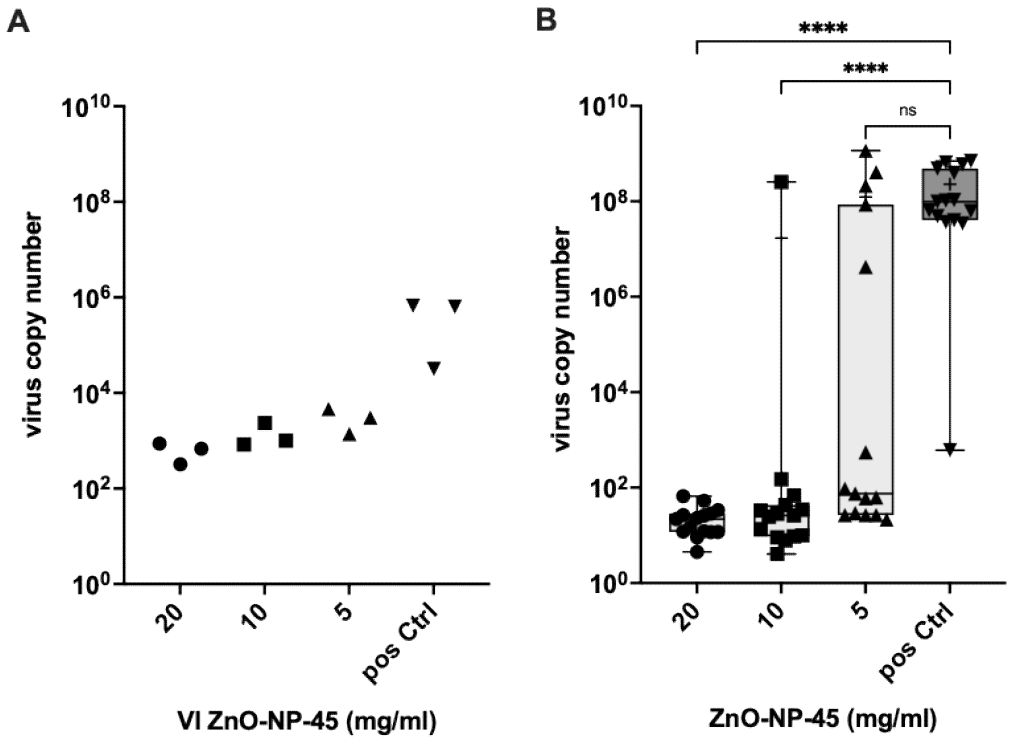

Figure 7 Virus neutralization assays using SARS-CoV-2 Delta.
A: Virus input (VI) used for cell infection after pre-incubation of SARS-CoV-2 Delta with ZnO-NP-45 for 1 h, followed by centrifugation, showing a concentration-dependent reduction in viral copies compared to the positive control (data from three independent experiments). B: Virus copies detected 48 h after infecting Calu-3 cells with the ZnO-NP-45 pretreated virus supernatant. Pretreatment with 20 mg/mL ZnO-NP-45 resulted in a virus inactivation exceeding 10^6-fold across all tested samples (three experimental series with five replicates each) compared to the positive control (untreated cells). Treatment with 10 mg/mL and 5 mg/mL of ZnO-NP-45 also decreased the number of infectious viruses, with inconsistent results among the replicates. p-values: > 0.05 = ns, ≤ 0.0001 = **** (Kruskal-Wallis test). Source: Wolfgruber et. al, 2023 (139).

5.2.2. ZnO-NP-76

Similar to the effects observed with ZnO-NP-45, pre-incubation of the Delta variant with increasing concentrations of ZnO-NP-76 led to a dose-dependent decrease in viral copies in the VI after centrifugation in comparison to untreated positive controls (Figure 8A) (139).

This effect appeared to be concentration-dependent and consistent across all three assays and all ZnO-NPs. While the observed adsorption of virus particles to ZnO-NP-45 and ZnO-NP-76 was similar, their neutralizing activity differed. Pretreatment with 20 mg/ml ZnO-NP-76 showed a similar virus-neutralizing effect as the use of 10 mg/ml ZnO-NP-45 and reduced virus copies in the majority of experimental replicates, although not consistently in all samples (Figure 8B) (139).

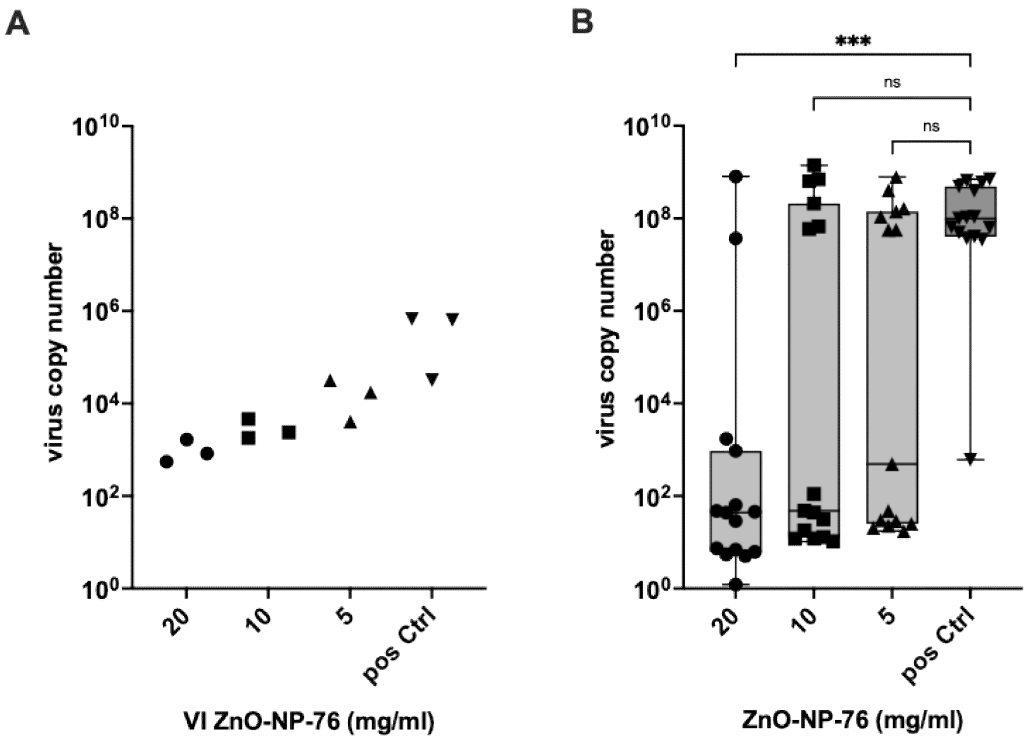

Figure 8 Virus neutralization assays using SARS-CoV-2 Delta.
A: Virus input (VI) used for cell infection after pre-incubation of SARS-CoV-2 Delta with ZnO-NP-76 for 1 h, followed by centrifugation, showing a concentration-dependent reduction in viral copies compared to the positive control (data from three independent experiments). B: Summary of virus copies detected 48 h after infection of Calu-3 cells with the virus-containing supernatant pretreated with ZnO-NP-76. p-values: > 0.05 = ns, ≤ 0.001 = *** (Kruskal-Wallis test). Wolfgruber et. al, 2023 (139).

5.2.3. ZnO-NP-ref

To evaluate the antiviral activity of ZnO-NP-45 and ZnO-NP-76 in comparison to the reference ZnO-NP (ZnO-NP-ref), an additional assay was done under the same experimental conditions as before. The reduction of virus particles in VI after pre-incubation with ZnO-NP-ref was similar to the other two NPs. However, due to technical issues, the VI in the positive control (Figure 9A) was lower than that observed in the assays with ZnO-NP-45 and ZnO-NP-76 (139). At concentrations of 20 mg/mL and 10 mg/mL, ZnO-NP-ref showed a virus-neutralizing effect comparable to ZnO-NP-76, reducing virus copies in some replicates, although not all (Figure 9B). At 5 mg/mL ZnO-NP-76 no virus neutralizing effect was observed.
Cells that were infected with the untreated virus (pos Ctrl) showed high copy numbers (139).

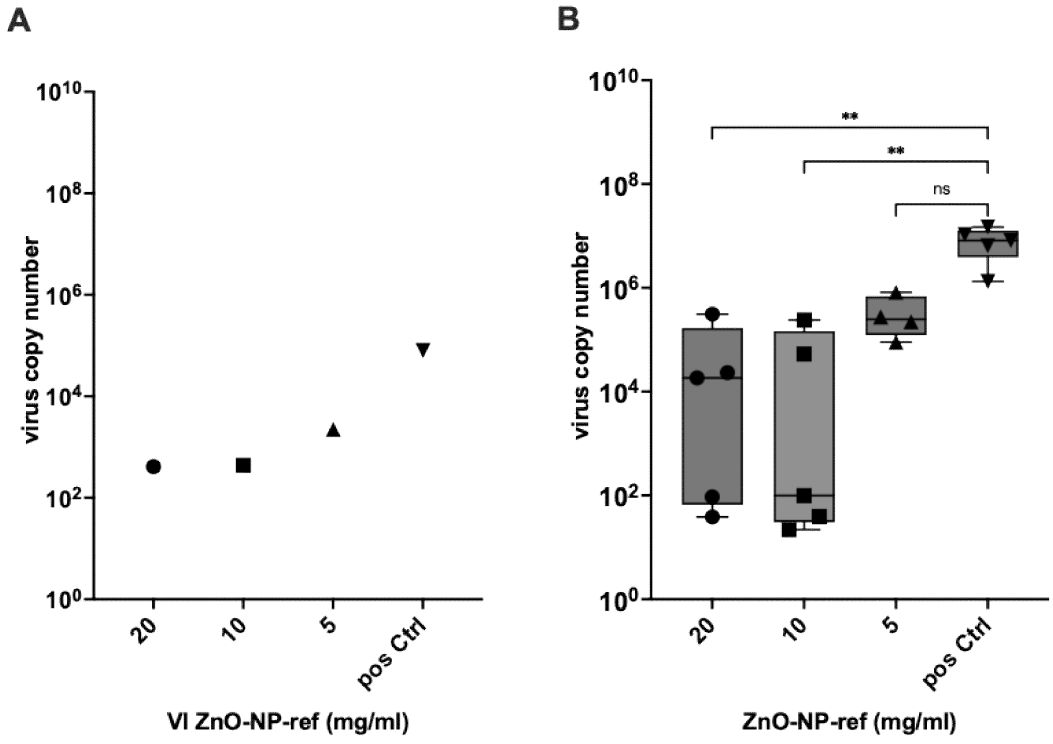

Figure 9 Virus neutralization assays using SARS-CoV-2 Delta.
A: Virus input (VI) used for cell infection after pre-incubation of SARS-CoV-2 Delta with ZnO-NP-ref for 1 h, followed by centrifugation, showing a concentration-dependent reduction in viral copies compared to the positive control. B: Virus copies detected 48 h after infection of Calu-3 cells with the virus-containing supernatant pretreated with ZnO-NP-ref. At NP concentrations of 20 mg/mL and 10 mg/mL infectious virus copies were reduced compared to the positive control (untreated cells), though not consistently in all replicates. No inactivating effect was observed with 5mg/mL ZnO-NP-ref. p-values: > 0.05 = ns, ≤ 0.01 = ** (Kruskal-Wallis test). Wolfgruber et. al, 2023 (139).

5.3. Antiviral activity of ZnO-NPs on SARS-CoV-2 Omicron

To determine whether the virus inactivation observed for SARS-CoV-2 Delta can also be used for the Omicron variant, a further neutralization assay was done using the same experimental conditions. To evaluated the virus-neutralizing activity of the ZnO-NPs two independent experimental methods were used for this assay. First, the virus copies in the cell culture supernatant were determined 48 h post infection using qRT-PCR. The infected cells were then labeled with an antibody directed against the SARS-CoV-2 nucleocapsid protein.

5.3.1. ZnP-NP-45

As already observed with the SARS-CoV-2 Delta variant, pre-incubation of the Omicron variant with the ZnO-NPs led to concentration-dependent decrease in viral copies in the supernatant, which was subsequently used as the VI for cell infection in the virus neutralization assays (Figure 10A) (139). When incubated with ZnO-NP-45 at 20 mg/mL and 10 mg/mL, virus replication was reduced by a factor of 10^6 in all samples after 48 h of cell culture, compared to the positive control cells infected with untreated virus (Figure 10B). At 5 mg/mL ZnO-NP-45, virus inactivation was observed in some replicates, but not all, with effects ranging from strong neutralization of infectious virus to high replication, similar to observations made with the Delta variant.

The observed low viral copy numbers 48 h after infection cannot be explained solely by the reduction of virus particles during pre-incubation and centrifugation, suggesting the involvement of additional antiviral mechanisms. This aligns with observations from previous experiments with SARS-CoV-2 Delta (139).

Immunohistochemical staining of the infected cells revealed that pretreatment with 20 mg/mL and 10 mg/mL ZnO-NP-45 resulted in no visible infected cells, which aligns with the antiviral effects observed in the qRT-PCR results (Figure 11). In samples treated with 5 mg/mL ZnO-NP-45, infected cells were visible in some wells, confirming the copy number calculations based on the qRT-PCR results. All wells of the positive control group were infected, while no infections were observed in the wells of the non-infected cells (negative control) (139).

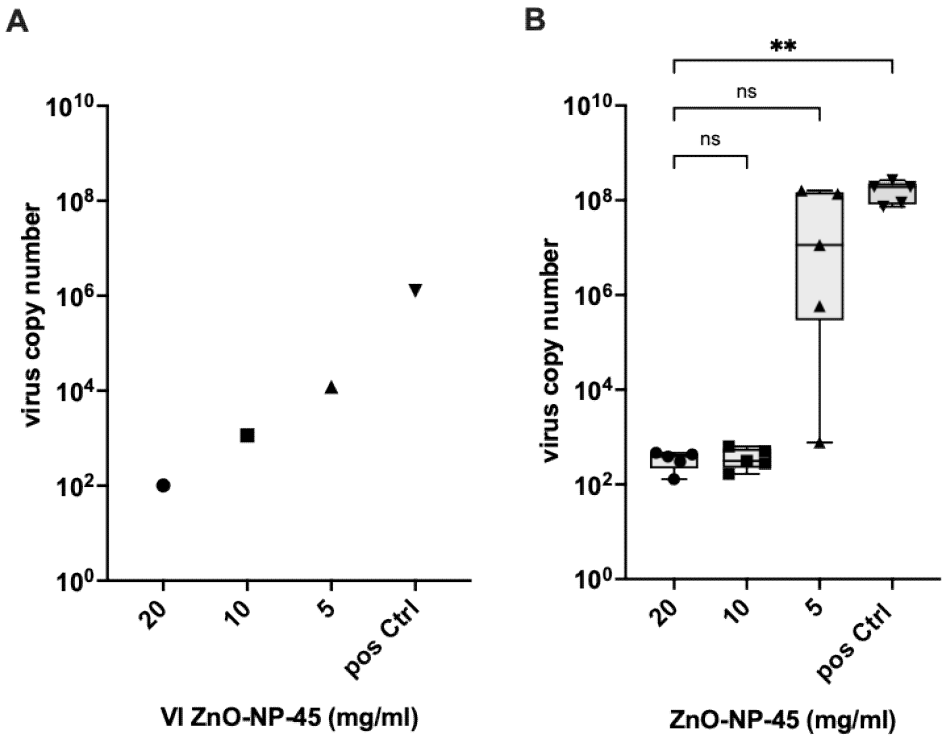

Figure 10 Virus neutralization assays using SARS-CoV-2 Omicron.
A: Virus input (VI) used for cell infection after pre-incubation of SARS-CoV-2 Omicron with ZnO-NP-45 for 1 h, followed by centrifugation, showing a concentration-dependent reduction in viral copies compared to the positive control. B: Virus copies in the supernatant 48 h after infection of Calu-3 cells with the virus-containing supernatant pretreated with ZnO-NP-45. At a NP concentration of 20 mg/mL and 10 mg/mL infectious virus copies were reduced by a factor of more than 10^6 in all tested samples compared to the positive control. At 5 mg/mL, infectious virus levels were also reduced, but not in all samples. *p*-values: > 0.05 = ns, ≤ 0.01 = ** (Kruskal-Wallis test). Wolfgruber et. al, 2023 (139).

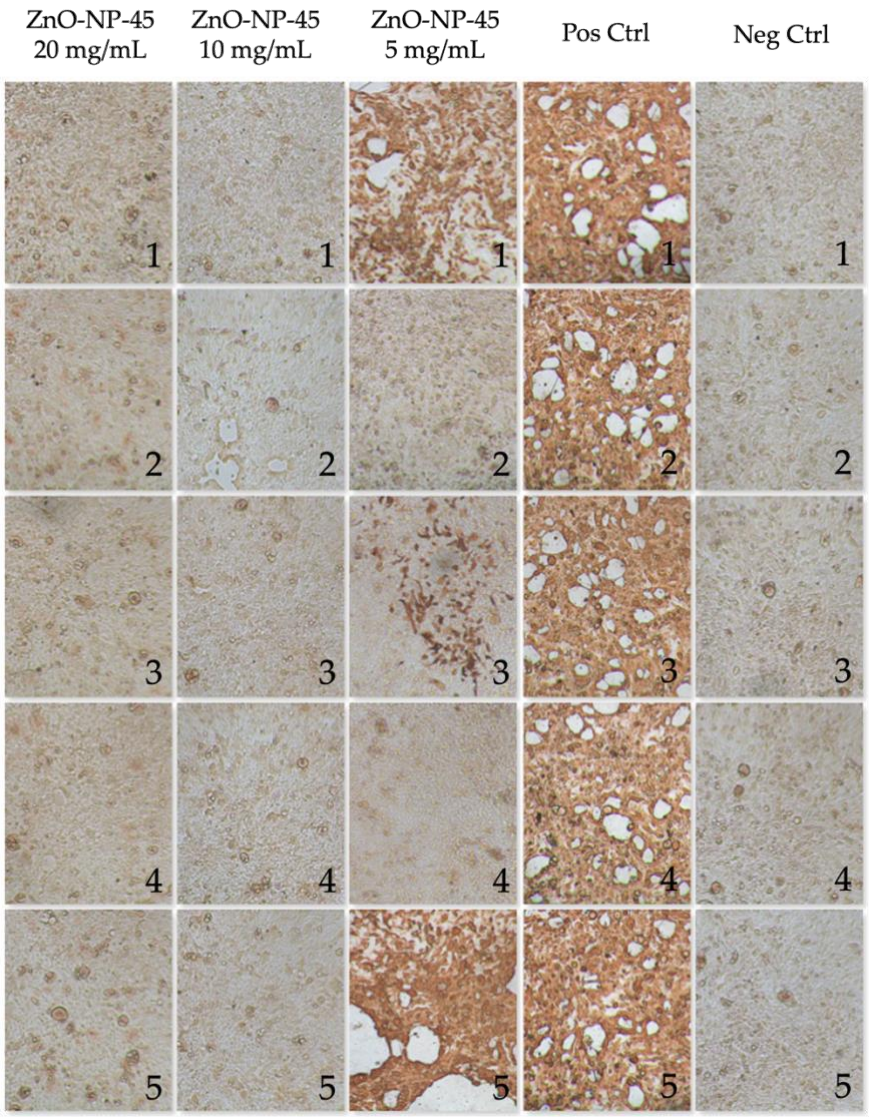

Figure 11 Antibody-stained Calu-3 cells after infection with SARS-CoV-2 Omicron pretreated with ZnO-NP-45.
Calu-3 cells stained with an antibody specific for the SARS-CoV-2 nucleocapsid protein 48 h after infection with virus samples pretreated with three different concentrations of ZnO-NP-45. Infected cells without NP pretreatment were used as positive control (Pos Ctrl), uninfected cells as negative control (Neg Ctrl). The numbers in the lower right corner of each panel represent the wells of each replicate for each concentration. After staining, virus-infected cells appear red. Magnification: 40×. Wolfgruber et. al, 2023 (139).

5.3.2. ZnO-NP-76

Pre-incubation of SARS-CoV-2 with ZnO-NP-76 reduced virus copies in the VI (Figure 12A), similar to the reduction seen with ZnO-NP-45 (Figure 10A). Pretreatment with ZnO-NP-76 resulted in comparable, but less consistent, virus inactivation compared to ZnO-NP-45.

Surprisingly, the highest virus inactivation was observed after pretreatment with 10 mg/mL ZnO-NP-76, which may be attributed to technical reasons as well as secondary infections in the samples preincubated with 20 mg/mL (139). Only a few still infectious virus copies can infect the entire well during the 48 h incubation period, resulting in high virus copy numbers.

For ZnO-NP-76 at 20 mg/mL and 5 mg/mL, immunohistochemical staining results aligned with the qRT-PCR findings, showing the presence of both infected and uninfected cells in the wells. No infected cells were detected following pre-incubation with 10 mg/mL ZnO-NP-76. All positive control wells were infected, while no infected cells were detected in the negative controls (Figure 13)(139).

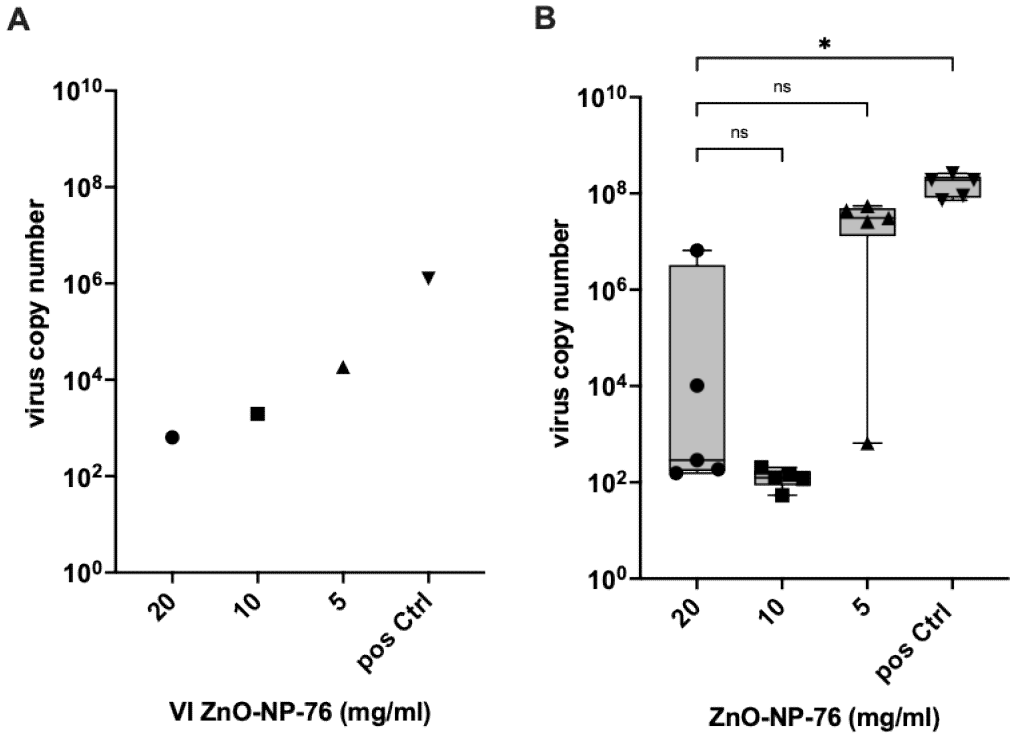

Figure 12 Virus neutralization assays using SARS-CoV-2 Omicron.
A: Virus input (VI) used for cell infection after pre-incubation of SARS-CoV-2 Omicron with ZnO-NP-76 for 1 h, followed by centrifugation, showing a concentration-dependent reduction in viral copies compared to the positive control. B: Pretreatment with ZnO-NP-76 at a concentration of 10 mg/mL reduced virus replication by a factor of 10^6 across all samples. Virus inactivation was observed in some replicates at concentrations of 20 mg/mL and 5 mg/mL, but not in all. *p*-values: > 0.05 = ns, ≤ 0.05 = * (Kruskal-Wallis test). Wolfgruber et. al, 2023 (139).

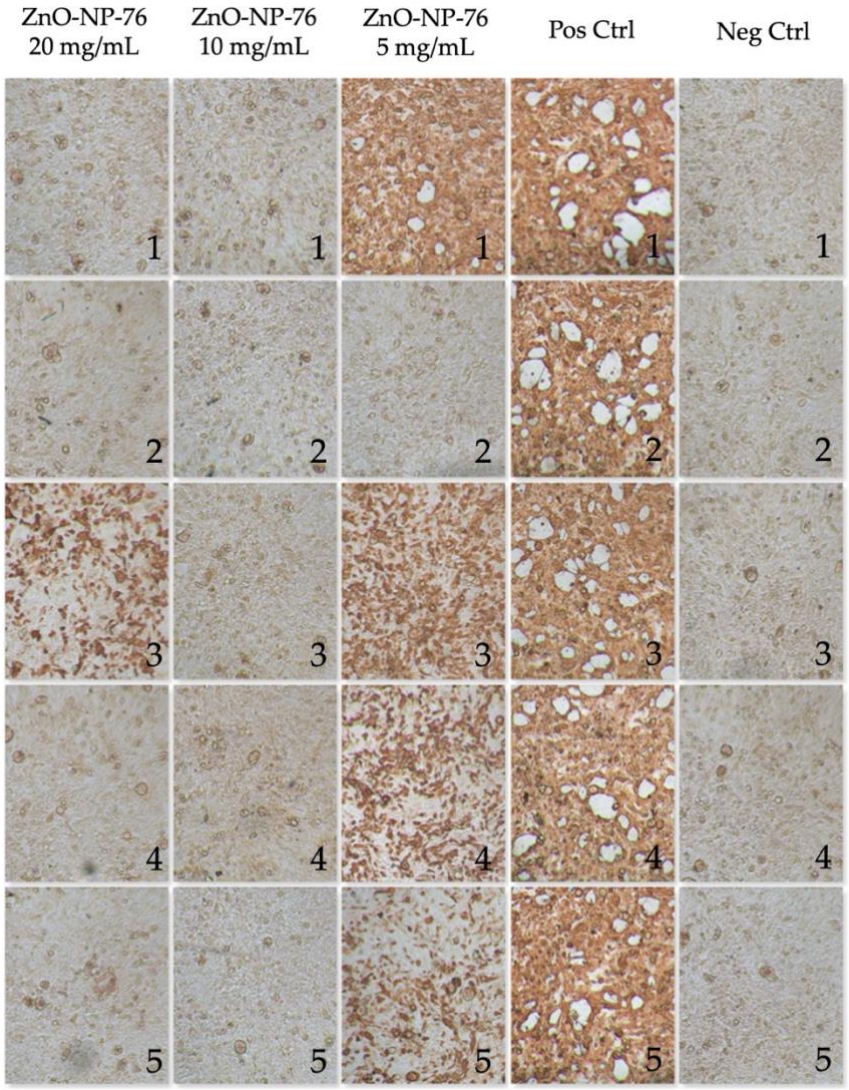

Figure 13 Antibody-stained Calu-3 cells after infection with SARS-CoV-2 Omicron pretreated with ZnO-NP-76.

Calu-3 cells stained with an antibody specific for the SARS-CoV-2 nucleocapsid protein 48 h after infection with virus samples pretreated with three different concentrations of ZnO-NP-76. Infected cells without NP pretreatment were used as positive control (Pos Ctrl), uninfected cells as negative control (Neg Ctrl). The numbers in the lower right corner of each panel represent the wells of each replicate for each concentration. After staining, virus-infected cells appear red. Magnification: 40×. Wolfgruber et. al, 2023 (139).

5.3.3. ZnO-NP-ref

A further series of control experiments was performed using the reference nanomaterial, ZnO-NP-ref, which resulted in the inactivation the Omicron variant across all tested samples at all three concentrations (Figure 14B). The reduction in virus particles in the VI (Figure 14A) was comparable to the results observed with ZnO-NP-45 and ZnO-NP-76 (139).

IHC staining confirmed these observations, as infected cells were not seen at any of the three ZnO-NP-ref concentrations, which correlates with the very low virus copy numbers from qRT-PCR (Figure 15). Control samples (infected cells without NP treatment and non-infected cells) were the same as for the other two NPs and are not shown here.

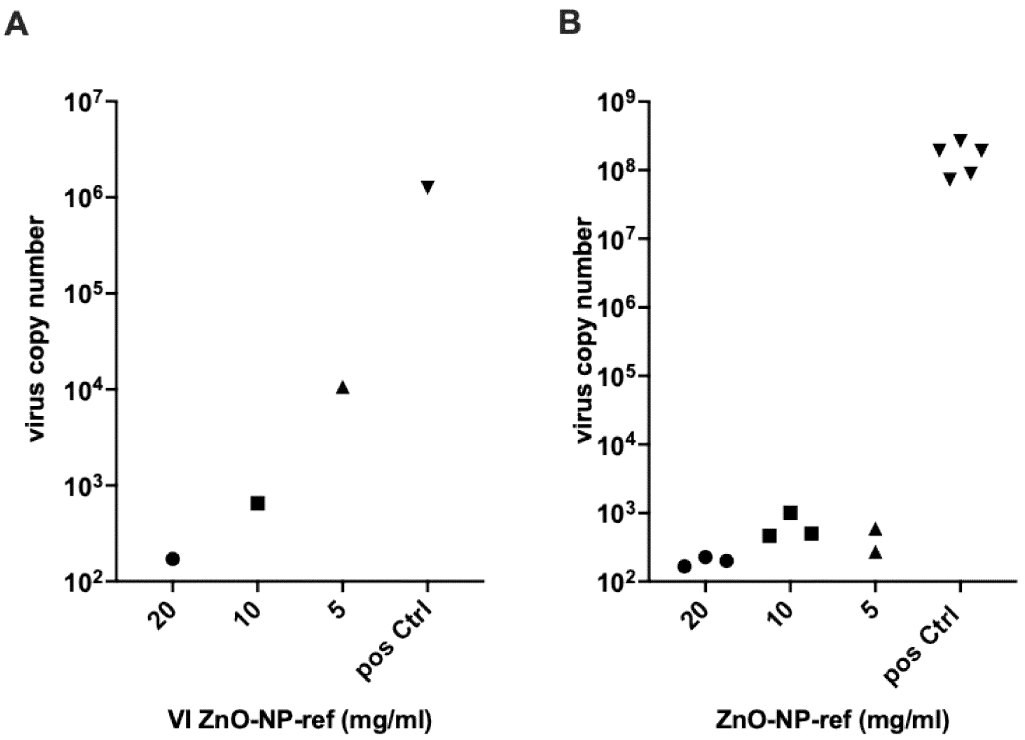

Figure 14 Virus neutralization assays using SARS-CoV-2 Omicron.
A: Virus input (VI) used for cell infection after pre-incubation of SARS-CoV-2 Omicron with ZnO-NP-ref for 1 h, followed by centrifugation, showing a concentration-dependent reduction in viral copies compared to the positive control. B: Virus copies after pretreatment with ZnO-NP-ref at three increasing concentrations 48 h after infection of the cells with the virus-containing supernatant. All tested concentrations led to a reduction in virus replication by approximately a factor 10^6. Wolfgruber et. al, 2023 (139).

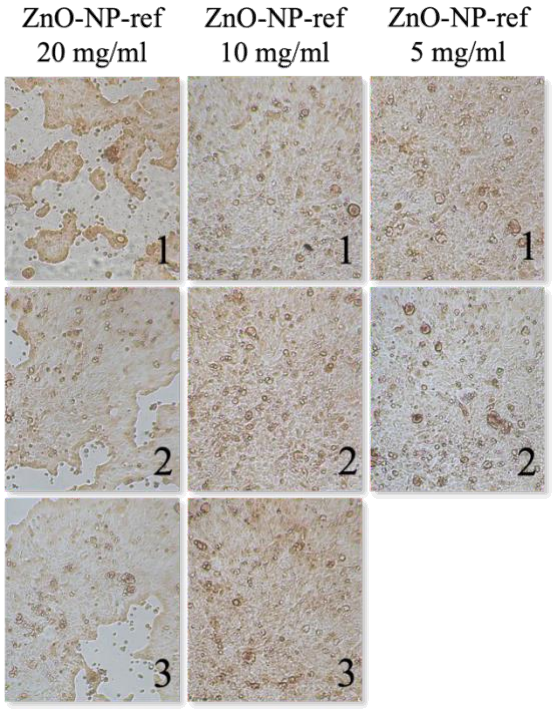

Figure 15 Antibody-stained Calu-3 cells after infection with SARS-CoV-2 Omicron pretreated with ZnO-NP-ref.
Calu-3 cells stained with an antibody specific for the SARS-CoV-2 nucleocapsid protein 48 h after infection with virus samples pretreated with three different concentrations of ZnO-NP-ref. The numbers in the lower right corner of each panel represent the wells of each replicate for each concentration. After staining, virus-infected cells appear red. Magnification: 40×. Wolfgruber et. al, 2023 (139).

5.4. Characterization of Zinc Oxide Nanoparticles

As observed during the virus neutralization assays, ZnO-NP-45 and ZnO-NP-76 showed differnet antiviral activity. At concentrations of 20 mg/mL and 10 mg/mL, ZnO-NP-45 demonstrated greater activity against SARS-CoV-2 Delta and Omicron compared to ZnO-NP-76. To investigate this difference, an extensive characterization of the nanoparticles was done. Since ZnO-NP-ref was used as the reference for all virus neutralization tests, it was also included in the characterization.

Characterization began with measuring the hydrodynamic size and zeta potential of the NPs using DLS, followed by visualization via STEM. Additionally, UV/Vis spectra were obtained, and Tauc plots were calculated from these data.

The hydrodynamic size and zeta potential of the ZnO-NPs were measured using DLS. All measurements are shown in Table 3 (139). The NP sizes were determined by DLS, weighted by number and intensity. The intensity-weighted size of ZnO-NP-45 (596.33 ± 29.10 nm) was much larger than the number-weighted size (193.17 ± 9.95 nm). This indicates the presence of agglomerates in the suspension. Larger particles are disproportionately represented in the intensity-weighted measurements due to the scattering intensity scaling with the particle size. The high PDI (0.65) shows that the suspension is highly polydisperse (139).

ZnO-NP-76 shows the largest intensity-weighted size (2125.33 ± 196.59 nm) and number-weighted size (1451.33 ± 20.17 nm), indicating that ZnO-NP-76 forms large agglomerates. However, the relatively small PDI (0.30) suggests that the size distribution within the agglomerates is relatively narrow and the particles are more uniform in size (139).

Similar to ZnO-NP-45, ZnO-NP-ref also exhibits a large difference between the intensity-weighted (678.27 ± 178.51 nm) and number-weighted (230.83 ± 42.25 nm) size, indicating agglomeration. The high PDI value (0.76) indicated the presence of highly polydisperse particles (139).

Both, ZnO-NP-45 and ZnO-NP-76 showed a positive zeta potential (28.87 ± 0.45 and 14.10 ± 0.20, respectively). The higher values for ZnO-NP-45 indicate that this NP should have better colloidal stability than ZnO-NP-76 due to the stronger electrostatic repulsion between the particles, which could reduce agglomeration under ideal conditions.

ZnO-NP-ref has a negative zeta potential (-1.69 ± 1.27 mV), which indicates poor colloidal stability. This could contribute to the stronger tendency to agglomerate observed in this sample. Although it is often reported that positively charged nanoparticles exhibit greater cytotoxicity than negatively charged ones (156), no cytotoxic effects were observed in our cell culture-based neutralization assays.

Table 3. Hydrodynamic size and zeta potential of ZnO-NP-45, ZnO-NP-76 and ZnO-NP-ref.
DLS: Mean ± SD values of intensity- and number-weighted distribution analyses from three independent measurements. Zeta potential: mean ± SD in mV of a suspension in Millipore water. PDI: Polydispersity index, which indicates the size homogeneity where 0 stands for uniform particle size and 1 for a highly polydisperse sample. Wolfgruber et. al, 2023 (139).

Sample	Size (nm) DLS Intensity	Size (nm) DLS Number	Zeta Potential (mV)	PDI
ZnO-NP-45	596.33 ± 29.10	193.17 ± 9.95	28.87 ± 0.45	0.65
ZnO-NP-76	2125.33 ± 196.59	1451.33 ± 20.17	14.10 ± 0.20	0.30
ZnO-NP-ref	678.27 ± 178.51	230.83 ± 42.25	−1.69 ± 1.27	0.76

STEM imaging of ZnO-NP-45 revealed a polydisperse mixture of particles with a size distribution of 45 ± 15 nm (Figure 16 A,B). In contrast, ZnO-NP-76 exhibited more uniform particles, with an average size of approximately 76 ± 16 nm (Figure 16C, D). Both ZnO-NPs were found agglomerate in suspension (139).

It is important to note that the observed particle sizes in the STEM images differ from those measured by DLS due to the differences between the two techniques. STEM captures the bare particle size by directly imaging the particles, while DLS measures the hydrodynamic radius in suspension, which includes both the particle and the surrounding solvent layer. This results in a larger size measurement with DLS, especially for agglomerated suspensions.

ZnO-NP-ref was not included in the STEM image analysis, so its detailed structural features could not be visualized. All STEM images of the NPs are shown with the highest possible magnification.

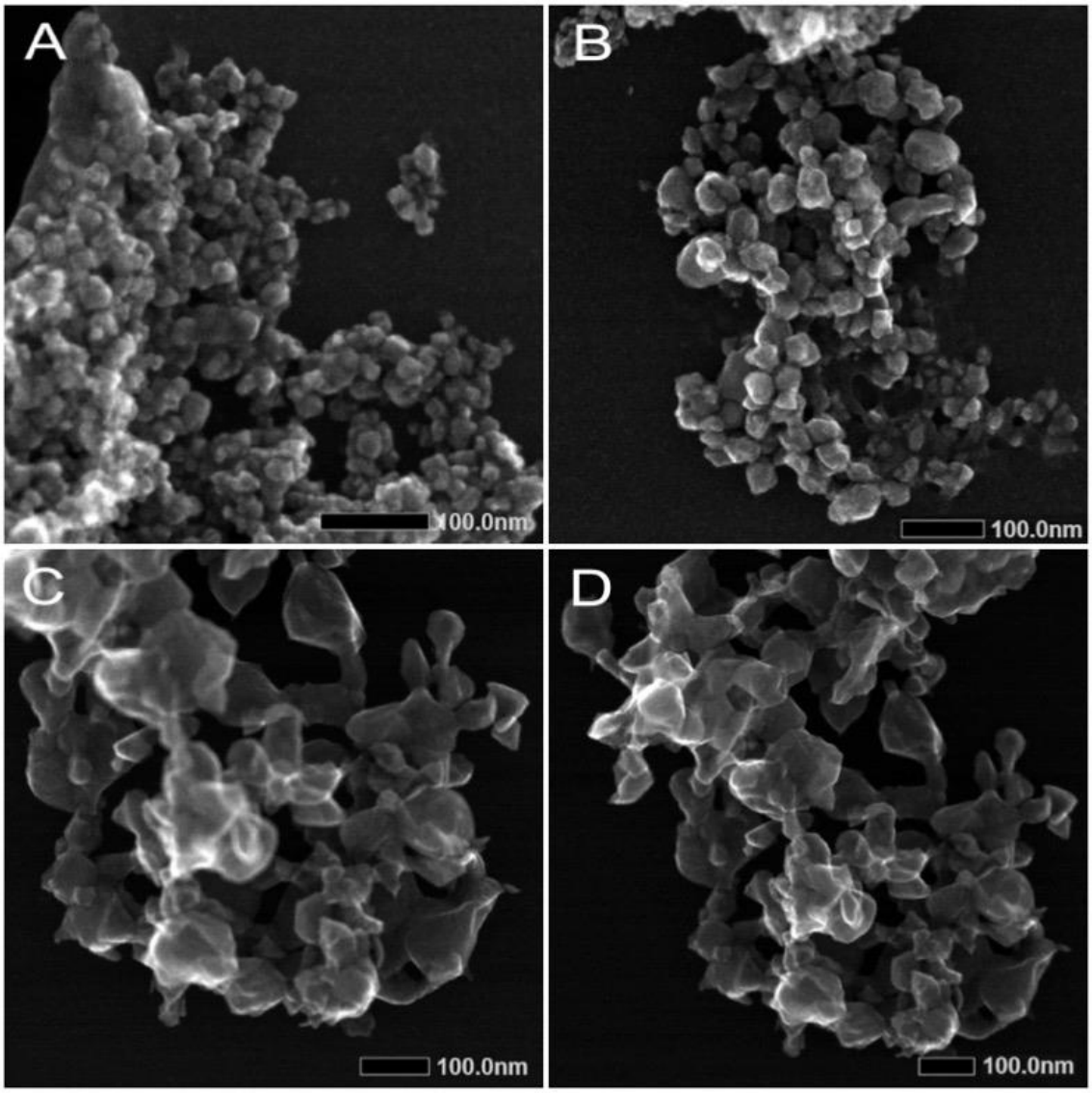

Figure 16 Scanning Transmission Electron Microscopy (STEM) images of ZnO-NPs.
STEM images show ZnO-NP-45 (A, B) and ZnO-NP-76 (C, D) in various sizes and aggregation states. Magnification: (A) 400,000×, (B) 300,000×, (C) 250,000×, (D) 200,000×, Scale bars: 100 nm. Wolfgruber et. al, 2023 (139).

The UV/Vis spectra of the NPs were recorded in the range of 350 nm to 800 nm at room temperature and showed a peak at 380 nm for all three NP preparations. UV/Vis spectroscopy is a widely used method to for determining nanoparticle sizes. For ZnO as a semiconductor, the initial and final absorbance wavelengths are strongly associated with the particle's band-gap, which decreases as the particle size increases.

When comparing the UV/Vis spectra of ZnO-NP-45 and ZnO-NP-76, ZnO-NP-45 shows a more rapid decrease in absorbance as the wavelength increases. This suggests that ZnO-NP-45 contains smaller NPs than ZnO-NP-76 (Figure 17A). The spectrum of ZnO-NP-ref was similar

to that of ZnO-NP-45. According to the manufacturer, the particles were all under 100 nm, but no further details on size distribution were provided.

To experimentally determine the band gap energy of the three nanomaterials the Tauc plot was used. The linear region of the curves was marked with dotted lines. ZnO-NP-45 has a bandgap energy of 3.06 eV, ZnO-NP-76 has 2.85 eV and ZnO-NP-ref has 2.99 eV (Figure 17B).

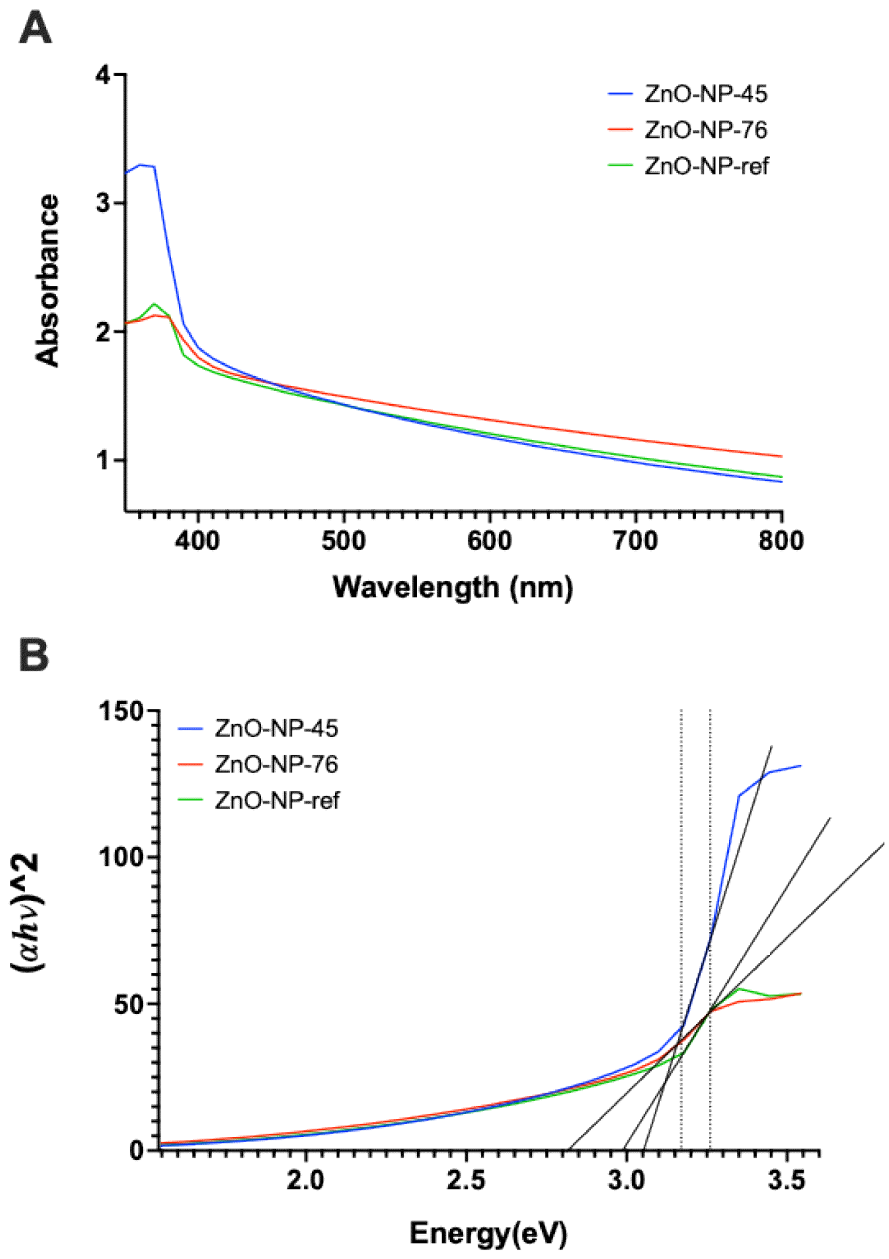

Figure 17 UV-VIS spectra of the three ZnO-NPs and Tauc plot.
(A) UV/Vis absorbance spectra of the three different ZnO-NPs at 3 mg/ml in PBS. Spectra are shown from 350-800 nm. (B) Tauc plot for experimental determination of direct bandgap.

The size and colloidal stability of ZnO-NP-45 and ZnO-NP-76 may explain their differences in antiviral activity. ZnO-NP-45, with smaller particles, better colloidal stability, and a higher surface area, likely interacts more effectively with the virus, resulting in stronger antiviral effects. In contrast, ZnO-NP-76 forms larger agglomerates, has a lower zeta potential, and less surface area for interaction, leading to reduced antiviral activity. These characteristics suggest that smaller, more stable nanoparticles are more effective in neutralizing the virus.

5.5. ROS measurement

All three ZnO-NPs showed antiviral activity as observed in the virus neutralization assays. The virus particles in the VI used for cell infection were reduced by adsorption to the NPs and centrifugation compared to the positive control (virus without NP pre-incubation). The high antiviral activity can be partly explained by this loss of virus particles, but there has to be another antiviral effect of the NPs to achieve virus inactivation by a factor of 10^6 as observed during the assays. One possible explanation could be the production of ROS by the NPs. To investigate this, the amount of ROS produced during incubation of the ZnO-NPs was measured. Since ROS can be generated either chemically or via photocatalysis, the same experimental setup was used in darkness and with exposure to light (4200 lux). The ROS levels were measured using the fluorescent probes DHE and H_2DCFDA. DHE can be oxidized to superoxide and more reactive radicals, but reacts only slightly with hydrogen peroxide (151), while H_2DCFDA is used to detect all ROS, including hydrogen peroxide (152).

Each NP preparation was investigated in technical triplicates across two separate experiments. PBS with the respective indicator was used as a control. The combined results from two experiments are presented in Figure 18 and Figure 19 for each fluorescent compound.

When incubated in the dark with DHE, all three ZnO-NPs produced low levels of ROS, comparable to the control sample that contained no NPs (Figure 18A). However, when exposed to continuous light at 4200 lux, a slight increase in ROS production was observed for ZnO-NP-45 compared to the other two NPs and the control (Figure 18B).

Incubation in the dark with H_2DCFDA resulted in a slight, but not significant, ROS increase for ZnO-NP-45 compared to the other NPs and control samples (Figure 19A). In contrast, high ROS production was detected with H_2DCFDA for ZnO-NP-45 with exposure to 4200 lux. ZnO-NP-76 and ZnO-NP-ref showed no increased ROS production compared to the control sample without NPs (Figure 19B).

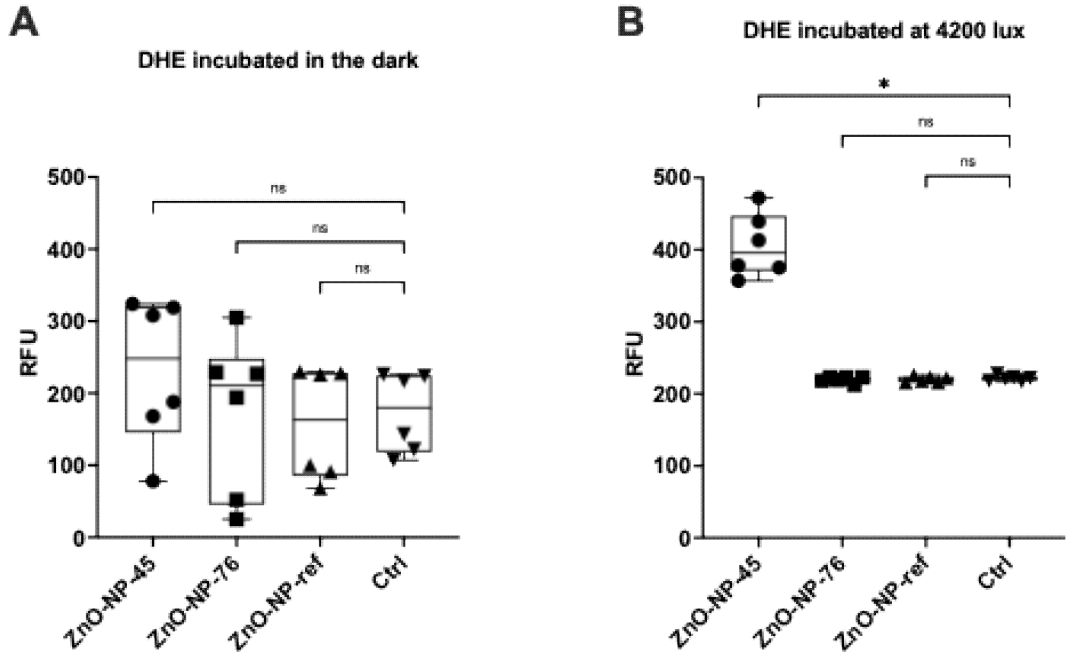

Figure 18 Fluorescence measurement of ROS using DHE.
(A) ZnO-NPs incubated with 5 µM DHE in the dark for 1 h at RT. No ROS production was detected compared to control. (B) ZnO-NPs incubated with 5 µM DHE at 4200 lux for 1 h at RT. Slightly higher ROS production was observed for ZnO-NP-45 compared to control. P-values: >0.05=ns, ≤ 0.05=* (Kruskal-Wallis test).

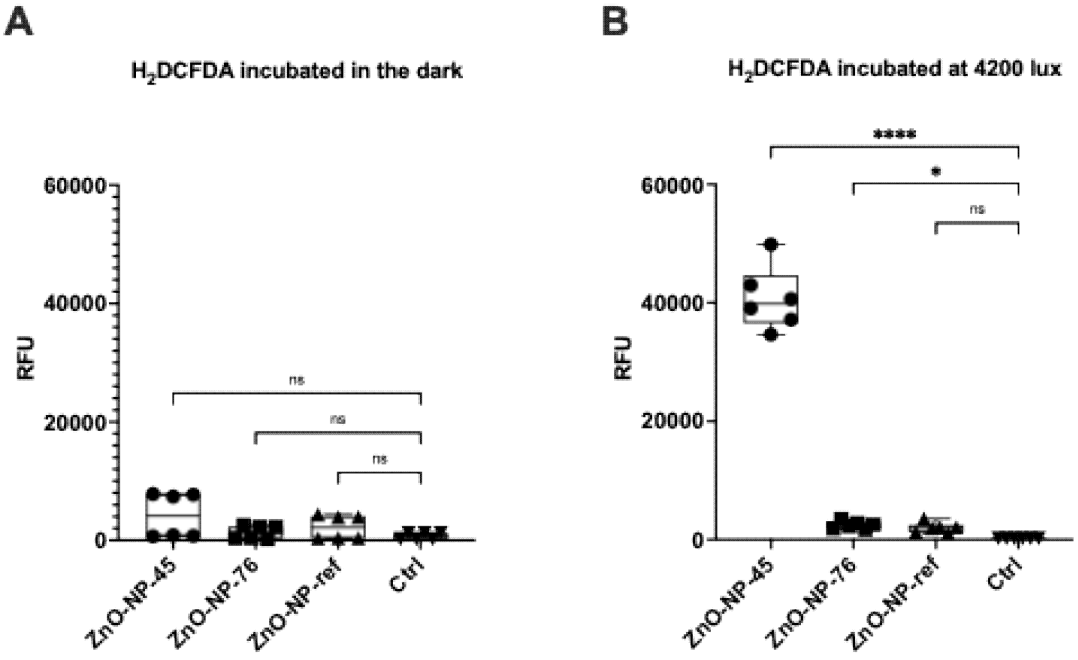

Figure 19 Fluorescence measurement of ROS using H_2DCFDA.
(A) ZnO-NPs incubated with 5 µM H_2DCFDA in the dark for 1 h at RT. No significant ROS production was detected. (B) ZnO-NPs incubated with 5 µM H_2DCFDA at 4200 lux for 1 h at RT. High ROS production was detected for ZnO-NP-45 compared to other NPs and control. P-values: >0.05=ns, ≤ 0.05=*, ≤ 0.0001**** (Kruskal-Wallis test).

5.6. BET surface area determination

The results of the BET surface area determination for the two ZnO-NPs are presented in Figure 20 and
Figure 21. The figures show the plotted data as adsorption-desorption isotherms (A), and the linear portion used to calculate the specific surface area of the ZnO-NPs (B). The x-axis represents the relative pressure, while the y-axis represents the adsorbed volume. ZnO-NP-45 has a specific surface area of 28 m^2/g, whereas ZnO-NP-76 has a much smaller specific surface area of 13.5 m^2/g. The higher ROS production of ZnO-NP-45 under constant light exposure can be attributed to its larger specific surface area compared to ZnO-NP-76.

Although ZnO-NP-45 exhibits higher ROS levels under constant light exposure, this does not necessarily imply stronger antiviral activity. The observed antiviral effects are probably not determined by ROS, but rather by the adsorption of the virus to the NPs, the potential loss during centrifugation and the antiviral properties of zinc. Therefore, although ROS production may play a role in NP behavior, it is probably not the main factor for the antiviral effects observed in this study.

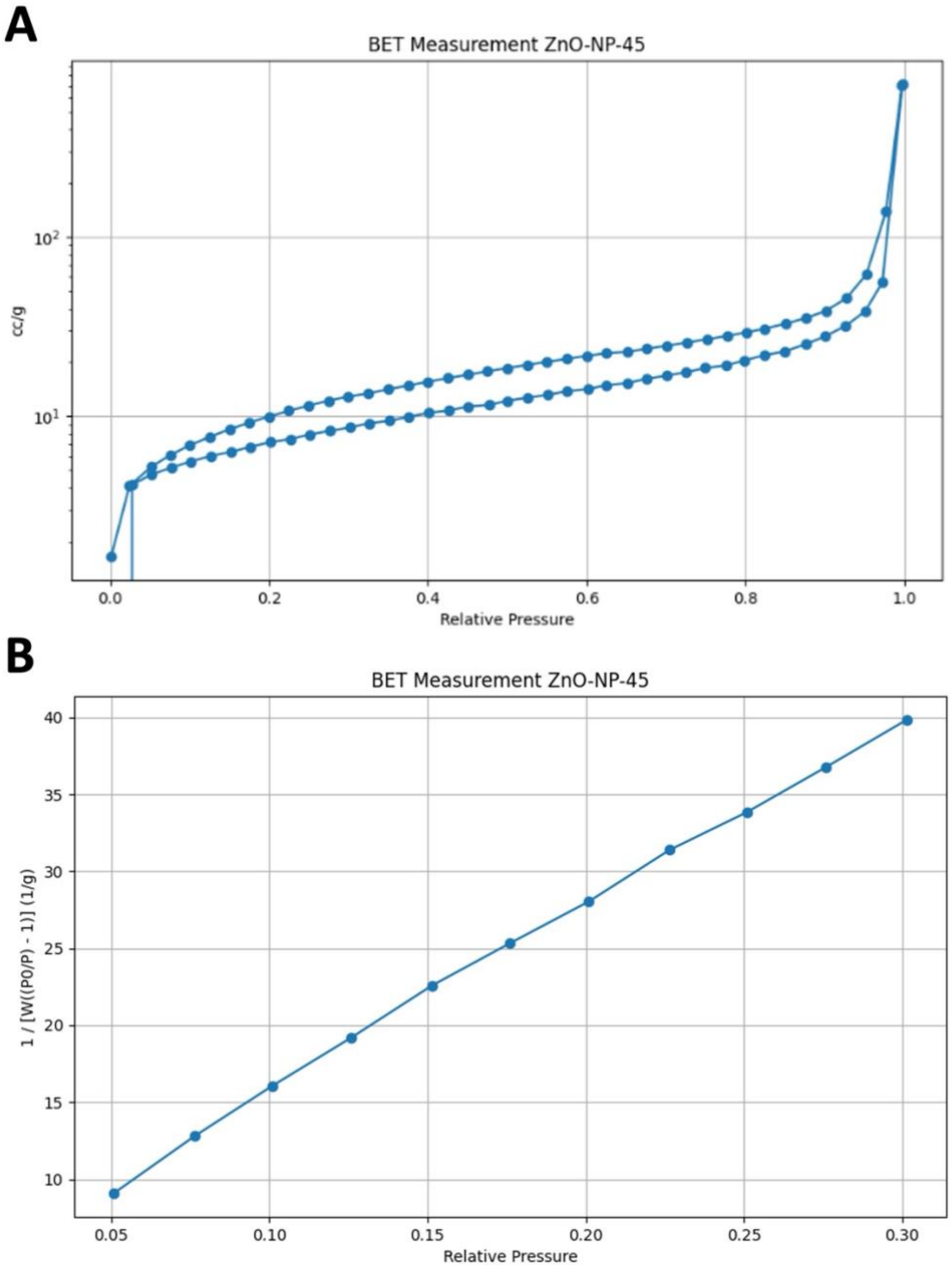

Figure 20 BET analysis of ZnO-NP-45.
(A) Adsorption/desorption isotherm plot, (B) BET plot of ZnO-NP-45 adsorption

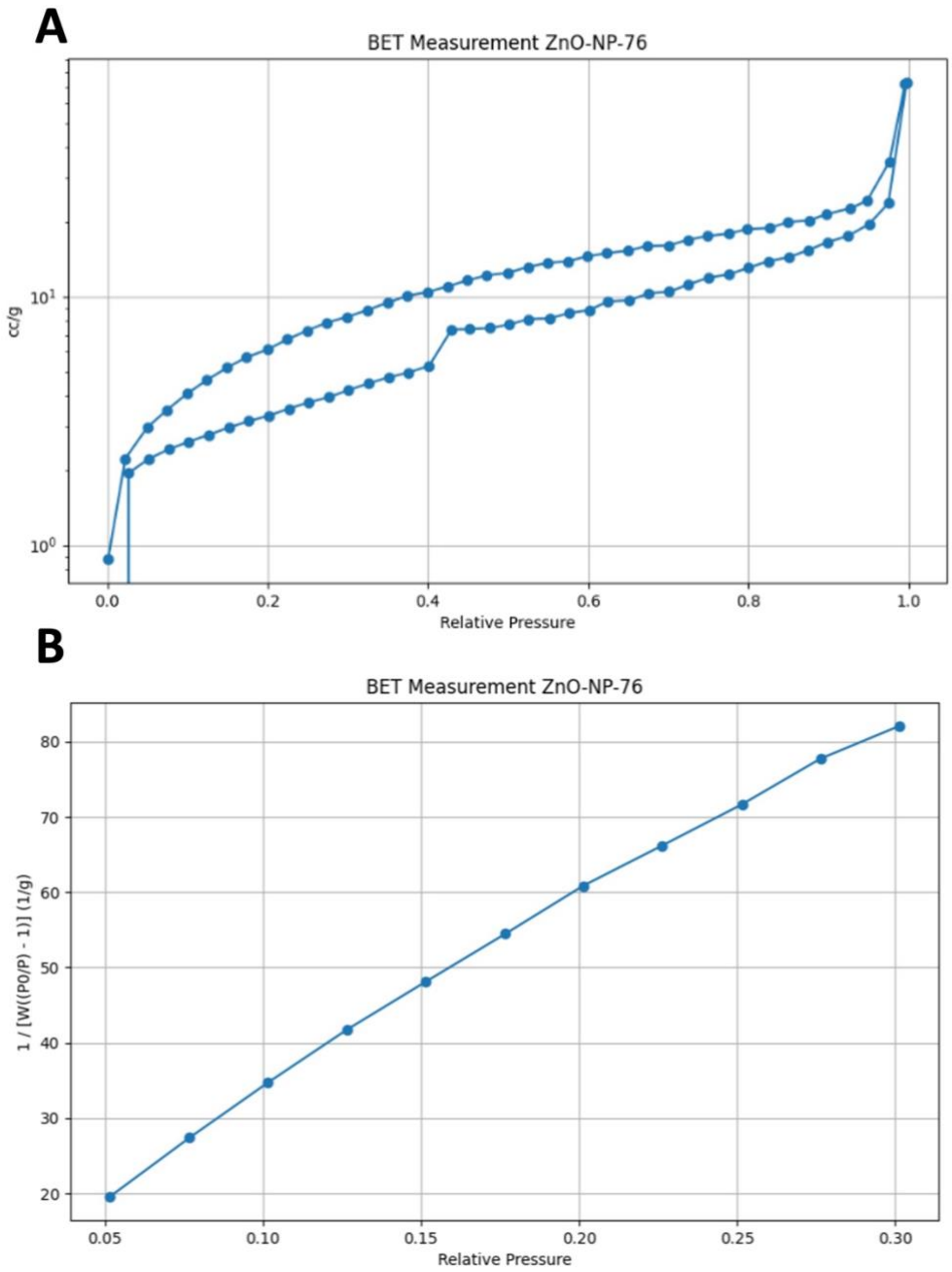

Figure 21 BET analysis of ZnO-NP-76.
(A) Adsorption/desorption isotherm plot, (B) BET plot of ZnO-NP-76 adsorption

6. Discussion

This study investigated the antiviral properties of two novel ZnO-NPs (ZnO-NP-45 and ZnO-NP-76) against SARS-CoV-2 Delta and Omicron, using several independent cell culture-based neutralization assays. Following this, a detailed characterization of the NPs was done to better understand their antiviral activities. These ZnO-NPs are of great interest due to their unique physical and chemical properties, their proven low cytotoxicity and their environmentally friendly production process.

Importantly, the production process of the ZnO-NPs used natural, abundant materials such as salts (nitrates, chlorates, and sulfates) and whey, typically a by-product of the dairy industry, as a chelating agent instead of conventional chemical reagents. This offers a new, more environmentally friendly synthesis method that reduces reliance on harmful chemicals and meets the increasing demand for environmentally friendly nanotechnology applications.

The outcomes of the virus neutralization assays showed that both ZnO-NPs were active against SARS-CoV-2, with ZnO-NP-45 achieving an inactivation by a factor of up to 10^6 at a concentration of 20 mg/mL.

The high level of virus inactivation observed in this study exceeds the established standards for disinfectants. According to the Robert Koch Institute (RKI) and the German Association for the Control of Virus Diseases (DVV), a reduction in viral activity by at least a factor of 10^4 is necessary for a substance to be classified as an effective disinfectant (56). In this context, ZnO-NP-45 clearly surpasses these criteria. Lower concentrations of ZnO-NP-45 and ZnO-NP-76 also demonstrated a reduction in viral replication, although the inhibitory effects were not consistently observed across all samples. Notable, ZnO-NP-76 treatment led to large variations in viral inactivation at all tested concentrations, ranging from strong neutralization of infectious virus to high replication. This variability might be attributed to incomplete virus inactivation after ZnO-NP pretreatment, along with secondary infections occurring during the virus neutralization assays. During the 48 h incubation period of infected Calu-3 cells, even a small number of virus-replicating cells can produce enough virus particles to trigger secondary infections, leading to high viral load as detected by RT-qPCR and confirmed by IHC.

The use of ZnO-NP-ref also led to a reduction of infectious virus particles, but appeared to exhibit a stronger antiviral effect on SARS-CoV-2 Omicron, as illustrated in Figure 14.

The inactivation of infectious SARS-CoV-2 Omicron was consistently observed for all concentrations of ZnO-NP-ref and in all replicates. For SARS-CoV-2 Delta, however, the effect of ZnO-NP-ref appeared to be less consistent, as only a limited number of replicates were inactivated at all concentrations tested (Figure 9).

Virus pretreatment with ZnO-NPs resulted in the binding and co-precipitation of both the virus and ZnO-NPs following centrifugation. This interaction was found to be dose-dependent, leading to a reduction of the VI used for the infection assays compared to the positive control samples without ZnO-NP pretreatment. While pretreatment and centrifugation reduced virus copy numbers by up to a factor of 10^4, the overall decrease in virus replication reached a factor of up to 10^6, indicating that the ZnO-NPs not only adsorbed the virus but also contributed to its inactivation, suggesting a chemical antiviral effect.
ZnO-NP-ref also exhibited antiviral activity, as the decrease in viral replication could not only be attributed to particle loss in the VI after pre-incubation and following centrifugation. Although it is possible that ZnO-NPs that were not precipitated during centrifugation could have additional effects on the cells used in the neutralization assays, the metabolic interference assay ruled out major interference with cell function at NP concentrations of up to 20 mg/ml.

The neutralization assays revealed different antiviral effects between the NP preparations; however, the underlying mechanisms responsible for these differences could not be clarified by the cell culture experiments performed.
Unfortunately, little is known about the antiviral properties of ZnO-NPs, as most research has focused primarily on their antibacterial effects (66, 157-160). The exact mechanism behind the antibacterial activity of ZnO-NPs is not yet fully understood. However, it is assumed that a combination of mechanisms contributes to the reduction of cell viability, including interactions between the cell membrane and ZnO-NPs, the generation of ROS and the intracellular release of Zn^{2+} ions, which disrupt essential cellular functions (160).
In terms of antiviral activity, one possible mechanism of ZnO-NPs, consistent with the proposed antibacterial mechanism, could involve the hydrolysis and inactivation of SARS-CoV-2 bound to the alkaline surface of ZnO-NPs. This could destroy the viral proteins or membranes upon contact with the ZnO-NPs. Another observation has been reported for the H1N1 influenza virus.

Both uncoated and PEGylated ZnO-NPs have been shown to inhibit the intracellular replication of the H1N1 virus following cell infection, likely through a mechanism involving the release of Zn^{2+} ions (134). Although similar results have not yet been observed with SARS-CoV-2, a similar mechanism is to be expected and needs further research. Additionally, ROS, often generated through photocatalytic reactions, can damage viral proteins, lipids, carbohydrates and nucleic acids, contributing to viral inactivation (114).
These mechanisms could all potentially contribute to the inactivation of SARS-CoV-2, but there was no clear evidence of which chemical mechanism was responsible for the viral neutralization observed in our experiments. Therefore, in a next step, an extensive characterization of the particles was performed to better understand the reasons for these differences in antiviral activity. Characterization of ZnO-NPs required multiple techniques to fully capture their properties and behavior, with each method having its limitations.

The investigation of the ZnO-NPs included measurements of their hydrodynamic sizes, zeta potential, PDI and agglomeration state using DLS, followed by UV/Vis spectra and STEM.
DLS is the most frequently used technique to measure particle size and PDI by tracking how light scattering changes due to the movement of NPs in a suspension. While DLS is a highly quantitative method, it can be influenced by larger particles or aggregates, which scatter light more intensely than smaller particles, making accurate visualization of polydisperse samples challenging (161).

NPs can be directly visualized using microscopic imaging techniques such as STEM, which was used for this study. This technique provides high-resolution images at the nanoscale by sending an electron beam through a sample attached to a grid. However, STEM may introduce artifacts due to the vacuum environment and potential sample preparation issues (161).
Another simple and cost-effective technique used for the characterization of NPs, which was also used here, is UV-Vis spectroscopy. It is non-invasive and only requires minimal sample preparation. The method can be used to measure the light transmission of a sample in the ultraviolet (UV), visible (VIS) and near infrared (NIR) range (180-1100 nm) (162). For this study measurements from 350 to 800 nm were done.

Particle size measurements using DLS and STEM revealed that ZnO-NP-45 consisted of particles ranging from 20 nm to 80 nm in size, while ZnO-NP-76 was monodispersed with particles around 80 nm. Obtaining high-quality DLS data from dispersions with agglomerated NPs is difficult as the bigger agglomerates scatter too much light. This excessive scattering not only masks low intensity scattered light from smaller particles but also results in broadened peaks, reducing confidence in the data (99).

The increased virus binding and neutralization activity of ZnO-NP-45 could be a consequence of its larger total reactive surface area than that of ZnO-NP-76. Particle size estimations done with DLS differed from the results obtained via STEM. Utilizing the image analysis software ImageJ, we determined size distributions of the ZnO-NPs from STEM images. However, the size measurements from STEM did not correlate well with data from DLS. This discrepancy can be explained by the different methodologies of the two techniques. STEM is a number-based technique using dry samples in a vacuum, whereas DLS analyzes particles in solution and determines the hydrodynamic radius (R_H) of dispersed particles. In addition, STEM provides size estimates based on the projected surface area by electron transfer (99), whereas DLS takes into account the entire solvation envelope around the particles, resulting in larger size measurements. An advantage of DLS is the ability to measure a much larger number of particles (in the millions) than STEM, where typically only a few hundred particles are analyzed (99).

NPs in suspension, especially in complex environments like cell culture media, tend to form agglomerates (163), a phenomenon we observed consistently across all experimental setups involving these particles. The formation of aggregates increases the hydrodynamic radius of the NPs making them more prone to rapid sedimentation. This sedimentation affects the homogeneity of NP suspensions, which can affect experimental reproducibility and outcomes (161). The ZnO-NPs used in this study exhibited poor dispersion in the cell culture medium and fast sedimentation, leading to unstable suspensions and difficulties in standardizing experimental conditions. To address this issue, the NP suspensions were mixed immediately before each use, and during pretreatment, samples were shaken at 300 min^{-1} to keep the particles suspended and minimize precipitation prior to centrifugation.

It's important to note that the stability of NP suspensions also depends on the solvent properties. In simpler solvents such as water or PBS, the stability may be lower compared to more complex media like cell culture medium, which contains biomolecules that can contribute to stabilizing interactions (164). NPs in cell culture medium interact with the components present in the medium before coming into contact with cells. The medium is a buffered solution containing a number of biomolecules, including amino acids, ionic salts, and is typically supplemented with serum. These components influence the hydrodynamic behavior of the NPs. In particular, the addition of serum plays a crucial role, as serum proteins can form a protein envelope around the NPs, which alters their surface characteristics, size, and stability (161). For this reason, ZnO-NPs were applied to cells in media without serum. Serum (10 % FCS) was only added during the 48 h incubation period after the ZnO-NPs were removed from the cells. Furthermore, the high ion content of the medium can influence the colloidal and chemical properties of the NPs, including their zeta potential and tendency to aggregate (161). To avoid such effects all DLS measurements used for the characterization of the ZnO-NPs were performed in Millipore water, but it should be noted that in water the stability of the suspension is likely to differ from that in culture medium.

Using zeta potential measurements, it was possible to gain insights into the colloidal stability of the NPs. ZnO-NP-45 and ZnO-NP-76 exhibited positive zeta potentials (28.87 ± 0.45 mV and 14.10 ± 0.20 mV, respectively), indicating better colloidal stability compared to ZnO-NP-ref, which had a near-neutral zeta potential (-1.69 ± 1.27 mV).

Zeta potential values above 30 mV are generally considered to provide strong electrostatic repulsion, reducing agglomeration and leading to more stable suspensions under ideal conditions (165). While ZnO-NP-45, with a zeta potential of 28.87 mV, suggests better stability than ZnO-NP-76 and ZnO-NP-ref, the difference between ZnO-NP-45 and ZnO-NP-76 is not large, but still suggests some variation in stability. However, zeta potential alone is not always sufficient to explain colloidal stability, as concentration also plays a role. The high concentrations of the ZnO-NP suspensions used here can increase the likelihood of particle collisions, which may lead to aggregation even if the zeta potential indicates good stability (165). These characteristics, including agglomeration and surface charge, could explain observed differences in their antiviral activity, as they influence how NPs interact with viral particles.

The high PDI value of ZnO-NP-45 (0.65) and the corresponding STEM images confirmed its polydispersity, indicating a wide range of particle sizes. Similarly, ZnO-NP-ref had an even higher PDI value (0.76), further demonstrating the presence of highly polydisperse particles. In contrast, the lower PDI of ZnO-NP-76 (0.30) suggested a narrower size distribution and greater uniformity within the agglomerates.

The differences in particle size distribution and agglomeration behavior of the ZnO-NPs are likely influencing their antiviral activity. The smaller size of ZnO-NP-45, greater surface area per weight and potential for better colloidal stability might contribute to its enhanced antiviral activity. In contrast, although ZnO-NP-76 showed a more uniform size distribution and stability, it had an inconsistent antiviral effect, possibly due to its larger overall size, which could reduce surface interaction with viral particles.

Metal oxide-based nano-photocatalysts, such as zinc oxide, are often semiconductors and possess an energetic band gap between the valence band and the conduction band. This band gap energy describes the energy required to excite an electron from the valence band to the conduction band (85). The band gap of bulk ZnO is 3.44 eV at low temperatures and 3.37 eV at room temperature (166). However, the band gap energies of the three ZnO-NPs were found to be lower. ZnO-NP-45 had a bandgap energy of 3.06 eV, ZnO-NP-76 had 2.85 eV and ZnO-NP-ref had 2.99 eV. The observed blue shift in the absorption spectra of these ZnO-NPs compared to bulk ZnO can be attributed to their reduced size and increased surface-to-volume ratio, suggesting different behavior compared to bulk zinc oxide. When electrons are excited from the valence band to the conduction band, they create empty spaces or “holes” in the valence band. In water-based surroundings, these electrons and holes can interact with molecular oxygen and hydroxyl ions, respectively. This interaction leads to the creation of ROS, such as the superoxide anion radical ($O_2^{\bullet -}$) and the hydroxyl radical (•OH) (112).

To further investigate the mode of action of virus inactivation, ROS production by the three ZnO-based nanomaterials was determined using the two fluorescent compounds DHE and H_2DCFDA. Since ROS can be generated either chemically or via photocatalysis, the same experimental setup was used in darkness and with exposure to light. DHE can be oxidized for superoxide and more reactive radicals but reacts only slightly with hydrogen peroxide. In

contrast, H_2DCFDA is a general ROS indicator that reacts with a broader range of species, including hydrogen peroxide, hydroxyl radicals, and peroxynitrite.

In the dark, none of the three ZnO-NPs showed an increase in ROS production when incubated with DHE, suggesting that minimal or no superoxide formation occurs in the absence of light. When exposed to light, the observations made with DHE remained largely the same, with no increase in ROS levels for ZnO-NP-76 and ZnO-NP-ref. However, ZnO-NP-45 showed a slight increase in ROS production when exposed to light.
In contrast, high ROS levels were detected for ZnO-NP-45 using H_2DCFDA under 4200 lux light exposure. ZnO-NP-76 and ZnO-NP-ref showed no increased ROS production compared to the control sample without ZnO-NPs. Low ROS levels were measured in the darkness for all three ZnO-NPs. Since H_2DCFDA can detect H_2O_2, which does not react with DHE, it can be assumed that the major fraction of ROS produced by ZnO-NP-45 and ZnO-NP-76 is likely H_2O_2.

As shown previously, both ZnO-NP-45 and ZnO-NP-ref demonstrated high antiviral activity in cell culture experiments. While ZnO-NP-45 was active against SARS-CoV-2 Delta and Omicron variants at concentrations of 20 mg/mL, ZnO-NP-ref showed higher activity against SARS-CoV-2 Omicron. Since the virus neutralization experiments were not performed under constant light exposure, the production of ROS was probably not primarily involved in virus inactivation. However, the high ROS production observed with ZnO-NP-45 when exposed to light raises some questions for further research.
Although ROS might not contribute much to the antiviral effect in our settings, this property can be exploited to enhanced antiviral effects in the presence of light. For example, under exposure to UV light or visible light, ZnO-NP-45 could produce increased levels of ROS, potentially resulting in greater antiviral activity compared to the other ZnO-NPs. It is known that ROS are highly reactive and can damage multiple components of viruses, including phospholipids, proteins and nucleic acids (167).
Since SARS-CoV-2 is an enveloped virus, it is consequently more susceptible to ROS-induced damage, leading to loss of infectivity compared to non-enveloped viruses. The envelope, which plays a key role in maintaining viral structure and facilitating host cell entry, is an important target for ROS (168, 169).

In contrast, non-enveloped viruses, which lack this lipid bilayer, are more resistant to oxidative stress, as their protein capsids provide a more robust structure against ROS (170). Further experiments under BSL-3 conditions combining ZnO-NP treatment with light exposure could answer the question whether ROS production can be used to improve the antiviral activity against respiratory viruses such as SARS-CoV-2.

The different ROS production between the three ZnO-NPs was further investigated using the BET surface area determination. With this technique it is possible to determine the specific surface area of a NP which is defined as the surface area per unit mass or volume of the particle. This method measures gas adsorption on the surface, offering a quantitative evaluation of the surface area available for interactions.
The specific surface area is an important property of the NPs because it greatly impacts their reactivity, binding capacity and overall antiviral activity. For NPs the specific surface area increases as particle size decreases. This is because smaller particles have a higher ratio of surface atoms to bulk atoms, making more surface available for chemical reactions. NPs with a high specific surface area have enhanced activities because of their larger reactive surface area relative to their mass (171).

The BET surface area measurement supported the hypothesis that ZnO-NP-45 might produce more ROS because of its greater reactive surface area compared to ZnO-NP-76. Although this could be an explanation for the increased ROS formation, the greater antiviral activity of ZnO-NP-45 is most likely not due to ROS alone.
Instead, the increased antiviral activity of ZnO-NP-45 may be related to other mechanisms, such as the strong adsorption of virus particles on the NP surface and the loss during centrifugation in the neutralization assays. In addition, zinc exhibits strong antiviral properties such as the prevention of viral protein synthesis and the inhibition of host cell attachment (172). The large specific surface area of ZnO-NP-45 may further enhance the antiviral effect by maximizing the exposure of zinc ions to the virus and thus enhancing the overall inhibition. Optimizing the size of NPs and their surface functionalization could be a promising option for designing more potent antiviral agents that combine direct inactivation and ROS-mediated mechanisms.

One advantage of using ZnO-NPs is that they can be used against a wide range of viruses, not just SARS-CoV-2, due to their broad spectrum of antiviral properties (160). As observed in this study, ZnO-NPs generate ROS that can damage viral structures, and they can release Zn^{2+} ions that further damage viruses. Their ability to interfere with viral replication, attachment and entry into host cells makes them even more versatile. In addition, ZnO-NPs are stable under various environmental conditions and can be incorporated into antiviral coatings and materials, making them suitable for reducing infections with various respiratory viruses.

For future studies, it is important to consider that ZnO-NPs in suspension may behave differently than ZnO-NPs immobilized on a surface, particularly in applications such as antiviral surface coatings. The stability and antiviral efficacy of ZnO-NPs can be very different depending on whether they are freely dispersed in a liquid medium or fixed to a surface. In suspension, ZnO-NPs can interact with the surrounding medium, which can affect their dispersion, stability, and overall behavior. For instance, in a liquid medium, factors such as particle aggregation, the production of ROS, and the ability for direct contact with viral particles play important roles in determining antiviral activity. Aggregation can reduce the effective surface area of the NPs available for interaction with viruses, while ROS can contribute to their antiviral effects but may be influenced by the NPs dispersal state. However, if the ZnO-NPs are immobilized on a surface, they are exposed to other interactions. The arrangement of the NPs on a surface may limit their mobility and, consequently, their efficacy in viral neutralization.

Considering these differences, it is important to recognize that the current results obtained exclusively in suspension do not fully reflect the potential performance of ZnO-NPs when applied as a surface coating. This represents a potential limitation of the study and highlights the need for additional experiments evaluating ZnO-NPs under conditions more representative of their potential application as antiviral coatings.

ZnO-NP-45 shows great potential for antiviral surface coatings, which makes it promising for applications in personal protective equipment (PPE). This could be particularly interesting for the coating of PPE to minimize the risk of infection when doffing the PPE, where there is a risk of getting into contact with the contaminated outside of the material. In addition, coating the inside of protective suits could be useful to prevent the growth of harmful microorganisms when

the suits are worn for long periods, which poses a health risk to users (173, 174). Such coated protective suits could improve working conditions for health care workers in epidemic or pandemic situations where hot temperatures pose an additional threat, as was the case with outbreaks of the Ebola virus in Africa (175).

Antiviral coatings for filters or ventilation systems are another promising application for the ZnO-NPs. Respiratory viruses, such as SARS-CoV-2 are transmitted by droplets that are emitted when breathing, speaking/singing, coughing and sneezing. The size of the droplets depends on their generation mechanism and their site of origin (176). Various studies have shown a correlation between indoor relative humidity (RH) and the incidence of viral respiratory infections. As RH decreases, particularly during the winter months due to indoor heating, the risk of viral infections rises (177-180). Heating dries the air and reduces RH, while at the same time improving the viability of viruses and weakening immune defenses (181). Respiratory droplets, which range in size from sub micrometers to thousands of micrometers, behave differently when humidity changes. Larger droplets at high RH settle to the ground in less than a second (182), while at lower RH smaller droplets shrink and remain airborne longer. This extended airborne time increases viral viability, as smaller droplets evaporate quickly, keeping viruses suspended in the air. In contrast, during summer, when RH is higher, larger droplets have shorter travel distances and settle more quickly. In addition, higher humidity promotes the formation of ROS at the droplet interface, which are known for their disinfectant properties. As a result, viruses in the droplets are degraded by ROS, reducing the risk of infection during summer (183). Consequently, antiviral coatings in air filters, heating and ventilation systems could help reduce virus transmission, especially during the colder months when low RH keeps viruses airborne longer and reduces the formation of ROS, limiting natural disinfection.

In conclusion, the results of this work show a strong antiviral effect of ZnO-NP-45, although the exact mechanisms are still unclear. The enhanced antiviral activity of ZnO-NP-45 is probably due to its smaller size and larger surface area, which allow better interaction with virus particles. Although ZnO-NP-45 produced high amounts of ROS under light exposure, the neutralization assays were not performed under continuous light, suggesting that ROS may not be the main factor for the antiviral effects.

ZnO-NP-45, with its high antiviral activity and sustainable production process using natural materials like whey, shows promise for future applications, such as antiviral surface coatings for PPE and filters for air-conditioning and ventilation systems.

7. References

1. SeyedAlinaghi S, Mirzapour P, Dadras O, Pashaei Z, Karimi A, MohsseniPour M, et al. Characterization of SARS-CoV-2 different variants and related morbidity and mortality: a systematic review. Eur J Med Res. 2021;26(1):51.
2. Gattringer T, Fandler-Höfler S, Kneihsl M, Hofer E, Köle W, Schmidt R, et al. Hospital admissions of acute cerebrovascular diseases during and after the first wave of the COVID-19 pandemic: a state-wide experience from Austria. J Neurol. 2021;268(10):3584-8.
3. (WHO) WHO. Rolling updates on coronavirus disease (COVID-19) 2020 [Available from: https://www.who.int/emergencies/diseases/novel-coronavirus-2019/events-as-they-happen.
4. (WHO) WHO. Coronavirus disease 2019 (COVID-19) Situation Report – 56 2020 [Available from: https://www.who.int/docs/default-source/coronaviruse/situation-reports/20200316-sitrep-56-covid-19.pdf?sfvrsn=9fda7db2_6.
5. (WHO) WHO. Coronavirus disease (COVID-19) pandemic 2024 [Available from: https://www.who.int/emergencies/diseases/novel-coronavirus-2019.
6. (WHO) WHO. WHO Director-General Dr Tedros end of 2023 message: Keeping the hope for health alive 2023 [Available from: https://www.who.int/director-general/speeches/detail/who-director-general-dr-tedros-end-of-2023-message--keeping-the-hope-for-health-alive.
7. Harrison AG, Lin T, Wang P. Mechanisms of SARS-CoV-2 Transmission and Pathogenesis. Trends Immunol. 2020;41(12):1100-15.
8. Goldsmith CS, Miller SE, Martines RB, Bullock HA, Zaki SR. Electron microscopy of SARS-CoV-2: a challenging task. The Lancet. 2020;395(10238):e99.
9. Lu R, Zhao X, Li J, Niu P, Yang B, Wu H, et al. Genomic characterisation and epidemiology of 2019 novel coronavirus: implications for virus origins and receptor binding. Lancet. 2020;395(10224):565-74.
10. Wu C-r, Yin W-c, Jiang Y, Xu HE. Structure genomics of SARS-CoV-2 and its Omicron variant: drug design templates for COVID-19. Acta Pharmacologica Sinica. 2022;43(12):3021-33.
11. Chan JF, Kok KH, Zhu Z, Chu H, To KK, Yuan S, et al. Genomic characterization of the 2019 novel human-pathogenic coronavirus isolated from a patient with atypical pneumonia after visiting Wuhan. Emerg Microbes Infect. 2020;9(1):221-36.
12. Perlman S, Netland J. Coronaviruses post-SARS: update on replication and pathogenesis. Nat Rev Microbiol. 2009;7(6):439-50.
13. Rajpal VR, Sharma S, Sehgal D, Singh A, Kumar A, Vaishnavi S, et al. A comprehensive account of SARS-CoV-2 genome structure, incurred mutations, lineages and COVID-19 vaccination program. Future Virol. 2022.
14. Bianchi M, Benvenuto D, Giovanetti M, Angeletti S, Ciccozzi M, Pascarella S. Sars-CoV-2 Envelope and Membrane Proteins: Structural Differences Linked to Virus Characteristics? Biomed Res Int. 2020;2020:4389089.
15. Ye G, Lin H, Chen S, Wang S, Zeng Z, Wang W, et al. Environmental contamination of SARS-CoV-2 in healthcare premises. J Infect. 2020;81(2):e1-e5.
16. Ding S, Liang TJ. Is SARS-CoV-2 Also an Enteric Pathogen With Potential Fecal-Oral Transmission? A COVID-19 Virological and Clinical Review. Gastroenterology. 2020;159(1):53-61.

17. Tian Y, Rong L, Nian W, He Y. Review article: gastrointestinal features in COVID-19 and the possibility of faecal transmission. Aliment Pharmacol Ther. 2020;51(9):843-51.
18. The species Severe acute respiratory syndrome-related coronavirus: classifying 2019-nCoV and naming it SARS-CoV-2. Nat Microbiol. 2020;5(4):536-44.
19. Shereen MA, Khan S, Kazmi A, Bashir N, Siddique R. COVID-19 infection: Origin, transmission, and characteristics of human coronaviruses. J Adv Res. 2020;24:91-8.
20. Lauer SA, Grantz KH, Bi Q, Jones FK, Zheng Q, Meredith HR, et al. The Incubation Period of Coronavirus Disease 2019 (COVID-19) From Publicly Reported Confirmed Cases: Estimation and Application. Ann Intern Med. 2020;172(9):577-82.
21. Alimohamadi Y, Sepandi M, Taghdir M, Hosamirudsari H. Determine the most common clinical symptoms in COVID-19 patients: a systematic review and meta-analysis. J Prev Med Hyg. 2020;61(3):E304-e12.
22. Mohamadian M, Chiti H, Shoghli A, Biglari S, Parsamanesh N, Esmaeilzadeh A. COVID-19: Virology, biology and novel laboratory diagnosis. J Gene Med. 2021;23(2):e3303.
23. Castanares-Zapatero D, Chalon P, Kohn L, Dauvrin M, Detollenaere J, Maertens de Noordhout C, et al. Pathophysiology and mechanism of long COVID: a comprehensive review. Ann Med. 2022;54(1):1473-87.
24. Carfì A, Bernabei R, Landi F. Persistent Symptoms in Patients After Acute COVID-19. Jama. 2020;324(6):603-5.
25. Payne S. 3 - Virus interactions with the cell. In: Payne S, editor. Viruses (Second Edition): Academic Press; 2023. p. 25-37.
26. Payne S. Chapter 3 - Virus Interactions With the Cell. In: Payne S, editor. Viruses: Academic Press; 2017. p. 23-35.
27. Magden J, Kääriäinen L, Ahola T. Inhibitors of virus replication: recent developments and prospects. Appl Microbiol Biotechnol. 2005;66(6):612-21.
28. Strmiskova M, Desrochers GF, Shaw TA, Powdrill MH, Lafreniere MA, Pezacki JP. Chemical Methods for Probing Virus–Host Proteomic Interactions. ACS Infectious Diseases. 2016;2(11):773-86.
29. Gillen J, Nita-Lazar A. Experimental Analysis of Viral–Host Interactions. Frontiers in Physiology. 2019;10.
30. Institut RK. Anwendung der SARS-CoV-2 Varianten Nomenklatur der WHO durch das RKI last access 24.06.2024 [Available from: https://www.rki.de/DE/Content/InfAZ/N/Neuartiges_Coronavirus/Virologische_Basisdaten_Varianten_Nomenklatur.html.
31. Duong D. Alpha, Beta, Delta, Gamma: What's important to know about SARS-CoV-2 variants of concern? Cmaj. 2021;193(27):E1059-e60.
32. Pecho-Silva S, Barboza J, Navarro-Solsol A, Rodriguez-Morales A, Bonilla-Aldana D, Panduro-Correa V. SARS-CoV-2 Mutations and Variants: what do we know so far? Microbes, Infection and Chemotherapy. 2021;1:e1256.
33. Dwivedi R, Sharma P, Farrag M, Kim SB, Fassero LA, Tandon R, et al. Inhibition of SARS-CoV-2 wild-type (Wuhan-Hu-1) and Delta (B.1.617.2) strains by marine sulfated glycans. Glycobiology. 2022;32(10):849-54.
34. Scovino AM, Dahab EC, Vieira GF, Freire-de-Lima L, Freire-de-Lima CG, Morrot A. SARS-CoV-2's Variants of Concern: A Brief Characterization. Front Immunol. 2022;13:834098.

35. Kimura I, Kosugi Y, Wu J, Zahradnik J, Yamasoba D, Butlertanaka EP, et al. The SARS-CoV-2 Lambda variant exhibits enhanced infectivity and immune resistance. Cell Rep. 2022;38(2):110218.
36. Volz E, Mishra S, Chand M, Barrett JC, Johnson R, Geidelberg L, et al. Assessing transmissibility of SARS-CoV-2 lineage B.1.1.7 in England. Nature. 2021;593(7858):266-9.
37. Cetin M, Balci PO, Sivgin H, Cetin S, Ulgen A, Dörtok Demir H, et al. Alpha variant (B.1.1.7) of SARS-CoV-2 increases fatality-rate for patients under age of 70 years and hospitalization risk overall. Acta Microbiol Immunol Hung. 2021.
38. Pascall DJ, Vink E, Blacow R, Bulteel N, Campbell A, Campbell R, et al. The SARS-CoV-2 Alpha variant was associated with increased clinical severity of COVID-19 in Scotland: A genomics-based retrospective cohort analysis. PLOS ONE. 2023;18(4):e0284187.
39. Vassallo M, Manni S, Klotz C, Fabre R, Pini P, Blanchouin E, et al. Patients Admitted for Variant Alpha COVID-19 Have Poorer Outcomes than Those Infected with the Old Strain. J Clin Med. 2021;10(16).
40. Grint DJ, Wing K, Houlihan C, Gibbs HP, Evans SJW, Williamson E, et al. Severity of Severe Acute Respiratory System Coronavirus 2 (SARS-CoV-2) Alpha Variant (B.1.1.7) in England. Clin Infect Dis. 2022;75(1):e1120-e7.
41. Tegally H, Wilkinson E, Giovanetti M, Iranzadeh A, Fonseca V, Giandhari J, et al. Detection of a SARS-CoV-2 variant of concern in South Africa. Nature. 2021;592(7854):438-43.
42. Carabelli AM, Peacock TP, Thorne LG, Harvey WT, Hughes J, Peacock SJ, et al. SARS-CoV-2 variant biology: immune escape, transmission and fitness. Nat Rev Microbiol. 2023;21(3):162-77.
43. Sarkar M, Madabhavi I. SARS-CoV-2 variants of concern: a review. Monaldi Archives for Chest Disease. 2022;93(3).
44. Diseases NIoI. Brief report: new variant strain of SARS-CoV-2 identified in travelers from Brazil. National Institute of Infectious Diseases Tokyo, Japan; 2021.
45. Imai M, Halfmann PJ, Yamayoshi S, Iwatsuki-Horimoto K, Chiba S, Watanabe T, et al. Characterization of a new SARS-CoV-2 variant that emerged in Brazil. Proceedings of the National Academy of Sciences. 2021;118(27):e2106535118.
46. Isnaini N, Mardian Y, Lokida D, Budiono F, Butar-Butar DP, Arlinda D, et al. Mild reinfection with severe acute respiratory syndrome coronavirus 2 (SARS-CoV-2) Delta variant: First case report from Indonesia. Front Med (Lausanne). 2022;9:906469.
47. Dhawan M, Saied AA, Mitra S, Alhumaydhi FA, Emran TB, Wilairatana P. Omicron variant (B.1.1.529) and its sublineages: What do we know so far amid the emergence of recombinant variants of SARS-CoV-2? Biomed Pharmacother. 2022;154:113522.
48. Riddell S, Goldie S, Hill A, Eagles D, Drew TW. The effect of temperature on persistence of SARS-CoV-2 on common surfaces. Virol J. 2020;17(1):145.
49. Chan KH, Peiris JS, Lam SY, Poon LL, Yuen KY, Seto WH. The Effects of Temperature and Relative Humidity on the Viability of the SARS Coronavirus. Adv Virol. 2011;2011:734690.
50. Chin AWH, Poon LLM. Stability of SARS-CoV-2 in different environmental conditions - Authors' reply. Lancet Microbe. 2020;1(4):e146.
51. Schumm MA, Hadaya JE, Mody N, Myers BA, Maggard-Gibbons M. Filtering Facepiece Respirator (N95 Respirator) Reprocessing: A Systematic Review. Jama. 2021;325(13):1296-317.

52. Ludwig-Begall LF, Wielick C, Dams L, Nauwynck H, Demeuldre PF, Napp A, et al. The use of germicidal ultraviolet light, vaporized hydrogen peroxide and dry heat to decontaminate face masks and filtering respirators contaminated with a SARS-CoV-2 surrogate virus. J Hosp Infect. 2020;106(3):577-84.
53. Rutala WA, Weber DJ. Disinfection and Sterilization in Health Care Facilities: An Overview and Current Issues. Infect Dis Clin North Am. 2016;30(3):609-37.
54. StonyBrookUniversity. Sterilization, Disinfection, & Decontamination 2024 [Available from: https://ehs.stonybrook.edu/programs/laboratory-safety/biological-safety/STERILIZATION%20DISINFECTION%20DECONTAMINATION.
55. McKeen L. 1 - Introduction to Food Irradiation and Medical Sterilization. In: McKeen L, editor. The Effect of Sterilization on Plastics and Elastomers (Third Edition). Boston: William Andrew Publishing; 2012. p. 1-40.
56. Rabenau HF, Schwebke I, Blümel J, Eggers M, Glebe D, Rapp I, et al. Guideline for testing chemical disinfectants regarding their virucidal activity within the field of human medicine : as of December 1st, 2014 Prepared by the German Association for the Control of Virus Diseases (DVV) and the Robert Koch Institute (RKI). Bundesgesundheitsblatt Gesundheitsforschung Gesundheitsschutz. 2020;63(5):645-55.
57. CDC. Guideline for Disinfection and Sterilization in Healthcare Facilities, 2008 June 2024 [Available from: https://www.cdc.gov/infection-control/media/pdfs/guideline-disinfection-h.pdf?CDC_AAref_Val=https://www.cdc.gov/infectioncontrol/pdf/guidelines/disinfection-guidelines-H.pdf.
58. Lin Q, Lim JYC, Xue K, Yew PYM, Owh C, Chee PL, et al. Sanitizing agents for virus inactivation and disinfection. VIEW. 2020;1(2):e16.
59. Pettersson R. Protein localization and virus assembly at intracellular membranes. Current topics in microbiology and immunology. 1991;170:67-106.
60. Anderson-Coughlin B. Why are viruses with an envelope less stable on surfaces and more susceptible to disinfectants than viruses without an envelope? : University of Delaware; [Available from: https://www.udel.edu/content/dam/udelImages/canr/photography/anfs/cewer/enveloped-vs-unenveloped-virus.pdf.
61. Nuanualsuwan S, Cliver DO. Capsid functions of inactivated human picornaviruses and feline calicivirus. Applied and environmental microbiology. 2003;69(1):350-7.
62. McDonnell GE. Antisepsis, disinfection, and sterilization: types, action, and resistance: John Wiley & Sons; 2020.
63. Jeong EK, Bae JE, Kim IS. Inactivation of influenza A virus H1N1 by disinfection process. Am J Infect Control. 2010;38(5):354-60.
64. Tung G, Macinga D, Arbogast J, Jaykus LA. Efficacy of commonly used disinfectants for inactivation of human noroviruses and their surrogates. J Food Prot. 2013;76(7):1210-7.
65. Murali M, Kalegowda N, Gowtham HG, Ansari MA, Alomary MN, Alghamdi S, et al. Plant-Mediated Zinc Oxide Nanoparticles: Advances in the New Millennium towards Understanding Their Therapeutic Role in Biomedical Applications. Pharmaceutics. 2021;13(10).
66. Sirelkhatim A, Mahmud S, Seeni A, Kaus NHM, Ann LC, Bakhori SKM, et al. Review on Zinc Oxide Nanoparticles: Antibacterial Activity and Toxicity Mechanism. Nanomicro Lett. 2015;7(3):219-42.
67. Murali M, Mahendra C, Nagabhushan, Rajashekar N, Sudarshana MS, Raveesha KA, et al. Antibacterial and antioxidant properties of biosynthesized zinc oxide nanoparticles from

Ceropegia candelabrum L. - An endemic species. Spectrochim Acta A Mol Biomol Spectrosc. 2017;179:104-9.
68. Singh V, Yadav SS, Chauhan V, Shukla S, Vishnolia KK. Applications of Nanoparticles in Various Fields. In: Yadav D, Bansal A, Bhatia M, Hooda M, Morato J, editors. Diagnostic Applications of Health Intelligence and Surveillance Systems. Hershey, PA, USA: IGI Global; 2021. p. 221-36.
69. Sarkar J, Das S, Aich S, Bhattacharyya P, Acharya K. Antiviral potential of nanoparticles for the treatment of Coronavirus infections. J Trace Elem Med Biol. 2022;72:126977.
70. Galdiero S, Falanga A, Vitiello M, Cantisani M, Marra V, Galdiero M. Silver nanoparticles as potential antiviral agents. Molecules. 2011;16(10):8894-918.
71. Lin N, Verma D, Saini N, Arbi R, Munir M, Jovic M, et al. Antiviral nanoparticles for sanitizing surfaces: A roadmap to self-sterilizing against COVID-19. Nano Today. 2021;40:101267.
72. Meléndez-Villanueva MA, Morán-Santibañez K, Martínez-Sanmiguel JJ, Rangel-López R, Garza-Navarro MA, Rodríguez-Padilla C, et al. Virucidal Activity of Gold Nanoparticles Synthesized by Green Chemistry Using Garlic Extract. Viruses. 2019;11(12).
73. Li R, Cui L, Chen M, Huang Y. Nanomaterials for Airborne Virus Inactivation: A Short Review. Aerosol Science and Engineering. 2021;5(1):1-11.
74. Lara HH, Ayala-Nuñez NV, Ixtepan-Turrent L, Rodriguez-Padilla C. Mode of antiviral action of silver nanoparticles against HIV-1. J Nanobiotechnology. 2010;8:1.
75. Armstrong AM, Sobsey MD, Casanova LM. Disinfection of bacteriophage MS2 by copper in water. Applied Microbiology and Biotechnology. 2017;101(18):6891-7.
76. Broglie JJ, Alston B, Yang C, Ma L, Adcock AF, Chen W, et al. Antiviral Activity of Gold/Copper Sulfide Core/Shell Nanoparticles against Human Norovirus Virus-Like Particles. PLoS One. 2015;10(10):e0141050.
77. Kim JY, Lee C, Love DC, Sedlak DL, Yoon J, Nelson KL. Inactivation of MS2 coliphage by ferrous ion and zero-valent iron nanoparticles. Environmental science & technology. 2011;45(16):6978-84.
78. Lu L, Sun RW-Y, Chen R, Hui C-K, Ho C-M, Luk JM, et al. Silver nanoparticles inhibit hepatitis B virus replication. Antiviral therapy. 2008;13(2):253-62.
79. Joe YH, Park DH, Hwang J. Evaluation of Ag nanoparticle coated air filter against aerosolized virus: Anti-viral efficiency with dust loading. Journal of hazardous materials. 2016;301:547-53.
80. Szekeres GP, Németh Zn, Schrantz K, Németh Kn, Schabikowski M, Traber J, et al. Copper-coated cellulose-based water filters for virus retention. ACS omega. 2018;3(1):446-54.
81. Pandey NK, Chudal L, Phan J, Lin L, Johnson O, Xing M, et al. A facile method for the synthesis of copper–cysteamine nanoparticles and study of ROS production for cancer treatment. Journal of Materials Chemistry B. 2019;7(42):6630-42.
82. Han J, Chen L, Duan S-M, Yang Q-X, Yang M, Gao C, et al. Efficient and quick inactivation of SARS coronavirus and other microbes exposed to the surfaces of some metal catalysts. Biomedical and environmental sciences: BES. 2005;18(3):176-80.
83. Darkwah WK, Ao Y. Mini review on the structure and properties (photocatalysis), and preparation techniques of graphitic carbon nitride nano-based particle, and its applications. Nanoscale Research Letters. 2018;13(1):388.

84. Mazurkow JM, Yüzbasi NS, Domagala KW, Pfeiffer S, Kata D, Graule T. Nano-sized copper (oxide) on alumina granules for water filtration: effect of copper oxidation state on virus removal performance. Environmental science & technology. 2019;54(2):1214-22.
85. Pant B, Park M, Park S-J. Recent Advances in TiO2 Films Prepared by Sol-Gel Methods for Photocatalytic Degradation of Organic Pollutants and Antibacterial Activities. Coatings. 2019;9(10):613.
86. Ruiz-Hitzky E, Darder M, Wicklein B, Ruiz-Garcia C, Martín-Sampedro R, Del Real G, et al. Nanotechnology Responses to COVID-19. Adv Healthc Mater. 2020;9(19):e2000979.
87. Zhang C, Li Y, Shuai D, Shen Y, Wang D. Progress and challenges in photocatalytic disinfection of waterborne Viruses: A review to fill current knowledge gaps. Chemical Engineering Journal. 2019;355:399-415.
88. Soni V, Khosla A, Singh P, Nguyen VH, Le QV, Selvasembian R, et al. Current perspective in metal oxide based photocatalysts for virus disinfection: A review. J Environ Manage. 2022;308:114617.
89. Rai M, Deshmukh SD, Ingle AP, Gupta IR, Galdiero M, Galdiero S. Metal nanoparticles: The protective nanoshield against virus infection. Critical reviews in microbiology. 2016;42(1):46-56.
90. Brady-Estévez AS, Schnoor MH, Kang S, Elimelech M. SWNT− MWNT hybrid filter attains high viral removal and bacterial inactivation. Langmuir. 2010;26(24):19153-8.
91. Park K-T, Hwang J. Filtration and inactivation of aerosolized bacteriophage MS2 by a CNT air filter fabricated using electro-aerodynamic deposition. Carbon. 2014;75:401-10.
92. Miao H, Teng Z, Wang C, Chong H, Wang G. Recent Progress in Two-Dimensional Antimicrobial Nanomaterials. Chemistry–A European Journal. 2019;25(4):929-44.
93. Ye S, Shao K, Li Z, Guo N, Zuo Y, Li Q, et al. Antiviral activity of graphene oxide: how sharp edged structure and charge matter. ACS Applied Materials & Interfaces. 2015;7(38):21571-9.
94. Chen Y-N, Hsueh Y-H, Hsieh C-T, Tzou D-Y, Chang P-L. Antiviral activity of graphene–silver nanocomposites against non-enveloped and enveloped viruses. International journal of environmental research and public health. 2016;13(4):430.
95. Li Y, Zhang C, Shuai D, Naraginti S, Wang D, Zhang W. Visible-light-driven photocatalytic inactivation of MS2 by metal-free g-C3N4: Virucidal performance and mechanism. Water Research. 2016;106:249-58.
96. Cheng R, Shen L-j, Yu J-h, Xiang S-y, Zheng X. Photocatalytic inactivation of bacteriophage f2 with Ag3PO4/g-C3N4 composite under visible light irradiation: performance and mechanism. Catalysts. 2018;8(10):406.
97. Baig N, Kammakakam I, Falath W. Nanomaterials: a review of synthesis methods, properties, recent progress, and challenges. Materials Advances. 2021;2(6):1821-71.
98. Abid N, Khan AM, Shujait S, Chaudhary K, Ikram M, Imran M, et al. Synthesis of nanomaterials using various top-down and bottom-up approaches, influencing factors, advantages, and disadvantages: A review. Advances in Colloid and Interface Science. 2022;300:102597.
99. Bhattacharjee S. DLS and zeta potential - What they are and what they are not? J Control Release. 2016;235:337-51.
100. Instruments M. Zetasizer nano user manual. Malvern Instruments Ltd, Worcestershire WR14 1XZ, UK. 2007.

101. Jin L, Jarand CW, Brader ML, Reed WF. Angle-dependent effects in DLS measurements of polydisperse particles. Measurement Science and Technology. 2022;33(4):045202.
102. Rodriguez-Loya J, Lerma M, Gardea-Torresdey JL. Dynamic Light Scattering and Its Application to Control Nanoparticle Aggregation in Colloidal Systems: A Review. Micromachines (Basel). 2023;15(1).
103. Wiki AP. The principles of dynamic light scattering [Available from: https://wiki.anton-paar.com/at-de/das-prinzip-der-dynamischen-lichtstreuung/.
104. Knysh A, Sokolov P, Nabiev I. Dynamic Light Scattering Analysis in Biomedical Research and Applications of Nanoparticles and Polymers. Journal of Biomedical Photonics & Engineering. 2023:020203.
105. Jia Z, Li J, Gao L, Yang D, Kanaev A. Dynamic Light Scattering: A Powerful Tool for In Situ Nanoparticle Sizing. Colloids and Interfaces. 2023;7(1):15.
106. Sparks DL. Soil physical chemistry. Soil Science. 1988;145(3):231-2.
107. nanoComposix. Zeta Potential Measurements last access 01.07.2024 [Available from: https://nanocomposix.com/pages/zeta-potential-measurements.
108. Rizwan M, Gwenin C. Chapter 5 - Nanomaterials in renewable energy: UV-Visible spectroscopy characterization and applications. In: Devasahayam S, Hussain CM, editors. Nano Tools and Devices for Enhanced Renewable Energy: Elsevier; 2021. p. 103-20.
109. Car J, Krstulović N. Fitting Procedure to Reconstruct the Size Distribution and the Concentration of Silver Colloidal Nanoparticles from UV-Vis Spectra. Nanomaterials (Basel). 2022;12(19).
110. Makuła P, Pacia M, Macyk W. How To Correctly Determine the Band Gap Energy of Modified Semiconductor Photocatalysts Based on UV-Vis Spectra. J Phys Chem Lett. 2018;9(23):6814-7.
111. Zanatta AR. Revisiting the optical bandgap of semiconductors and the proposal of a unified methodology to its determination. Sci Rep. 2019;9(1):11225.
112. Saliani M, Jalal R, Goharshadi EK. Mechanism of oxidative stress involved in the toxicity of ZnO nanoparticles against eukaryotic cells. Nanomedicine Journal. 2016;3(1):1-14.
113. Kessler A, Hedberg J, Blomberg E, Odnevall I. Reactive Oxygen Species Formed by Metal and Metal Oxide Nanoparticles in Physiological Media-A Review of Reactions of Importance to Nanotoxicity and Proposal for Categorization. Nanomaterials (Basel). 2022;12(11).
114. Idrissa H, Habibb M, Alakhrasa A, El Khaira H, Vol B. ZnO nanoparticles and their properties as surface coating materials against coronavirus. Journal of Optoelectronic and Biomedical Materials. 2022;14(2):53-61.
115. Hayat MA. Principles and techniques of electron microscopy. Biological applications, volume 31973.
116. Malatesta M. Transmission Electron Microscopy as a Powerful Tool to Investigate the Interaction of Nanoparticles with Subcellular Structures. Int J Mol Sci. 2021;22(23).
117. Inc. TS. Scanning transmission electron microscopy last access 02.07.2024 [Available from: https://www.thermofisher.com/at/en/home/electron-microscopy/products/transmission-electron-microscopes.html.
118. Nanakoudis A. EDX Analysis with SEM: How does it work www.thermofisher.com2019 [Available from: https://www.thermofisher.com/blog/materials/edx-analysis-with-sem-how-does-it-work/.

119. Wisz G, Virt I, Sagan P, Potera P, Yavorskyi R. Structural, Optical and Electrical Properties of Zinc Oxide Layers Produced by Pulsed Laser Deposition Method. Nanoscale Res Lett. 2017;12(1):253.
120. Shaba EY, Jacob JO, Tijani JO, Suleiman MAT. A critical review of synthesis parameters affecting the properties of zinc oxide nanoparticle and its application in wastewater treatment. Applied Water Science. 2021;11(2):48.
121. Mandal AK, Katuwal S, Tettey F, Gupta A, Bhattarai S, Jaisi S, et al. Current Research on Zinc Oxide Nanoparticles: Synthesis, Characterization, and Biomedical Applications. Nanomaterials (Basel). 2022;12(17).
122. Code of Federal Regulations-21CFR182.8991 (FDA. 11 October 2022 [Available from: https://www.accessdata.fda.gov/scripts/cdrh/cfdocs/cfcfr/cfrsearch.cfm?fr=182.8991
123. Song Z, Kelf TA, Sanchez WH, Roberts MS, Rička J, Frenz M, et al. Characterization of optical properties of ZnO nanoparticles for quantitative imaging of transdermal transport. Biomed Opt Express. 2011;2(12):3321-33.
124. Kalpana VN, Devi Rajeswari V. A Review on Green Synthesis, Biomedical Applications, and Toxicity Studies of ZnO NPs. Bioinorg Chem Appl. 2018;2018:3569758.
125. Asif N, Fatima S, Siddiqui T, Fatma T. Investigation of morphological and biochemical changes of zinc oxide nanoparticles induced toxicity against multi drug resistance bacteria. J Trace Elem Med Biol. 2022;74:127069.
126. Mishra PK, Mishra H, Ekielski A, Talegaonkar S, Vaidya B. Zinc oxide nanoparticles: a promising nanomaterial for biomedical applications. Drug Discov Today. 2017;22(12):1825-34.
127. Sun Q, Li J, Le T. Zinc Oxide Nanoparticle as a Novel Class of Antifungal Agents: Current Advances and Future Perspectives. J Agric Food Chem. 2018;66(43):11209-20.
128. Ficociello G, De Caris MG, Trillò G, Cavallini D, Sarto MS, Uccelletti D, et al. Anti-Candidal Activity and In Vitro Cytotoxicity Assessment of Graphene Nanoplatelets Decorated with Zinc Oxide Nanorods. Nanomaterials (Basel). 2018;8(10).
129. abedzadeh hajar A, dakhili m, saghazadeh m, aghaei SS, Nazari R. Synergistic Antifungal Effect of Fluconazole Combined with ZnO Nanoparticles against Candida albicans Strains from Vaginal Candidiasis. Medical Laboratory Journal. 2020;14(3):26-32.
130. Xue J, Luo Z, Li P, Ding Y, Cui Y, Wu Q. A residue-free green synergistic antifungal nanotechnology for pesticide thiram by ZnO nanoparticles. Sci Rep. 2014;4:5408.
131. Korant BD, Kauer JC, Butterworth BE. Zinc ions inhibit replication of rhinoviruses. Nature. 1974;248(449):588-90.
132. Haraguchi Y, Sakurai H, Hussain S, Anner BM, Hoshino H. Inhibition of HIV-1 infection by zinc group metal compounds. Antiviral Res. 1999;43(2):123-33.
133. Gupta J, Irfan M, Ramgir N, Muthe KP, Debnath AK, Ansari S, et al. Antiviral Activity of Zinc Oxide Nanoparticles and Tetrapods Against the Hepatitis E and Hepatitis C Viruses. Front Microbiol. 2022;13:881595.
134. Ghaffari H, Tavakoli A, Moradi A, Tabarraei A, Bokharaei-Salim F, Zahmatkeshan M, et al. Inhibition of H1N1 influenza virus infection by zinc oxide nanoparticles: another emerging application of nanomedicine. J Biomed Sci. 2019;26(1):70.
135. Abbasi M, Arab-Bafrani Z, Zabihi E, Babaei A, Jafari SM, Barani M, et al. Inhibitory effect of zinc oxide nanoparticles and fibrillar chitosan-zinc oxide nanostructures against herpes simplex virus infection. The Journal of Engineering. 2023;2023(6):e12268.
136. Minaeian S, Khales P, Hosseini-Hosseinabad SM, Farahmand M, Poortahmasebi V, Habib Z, et al. Evaluation of Activity of Zinc Oxide Nanoparticles on Human Rotavirus and Multi-Drug Resistant Acinetobacter Baumannii. Pharm Nanotechnol. 2023;11(5):475-85.

137. Sportelli MC, Izzi M, Loconsole D, Sallustio A, Picca RA, Felici R, et al. On the Efficacy of ZnO Nanostructures against SARS-CoV-2. Int J Mol Sci. 2022;23(6).
138. Soares VA, Xavier MJS, Rodrigues ES, de Oliveira CA, Farias PMA, Stingl A, et al. Green synthesis of ZnO nanoparticles using whey as an effective chelating agent. Materials Letters. 2020;259:126853.
139. Wolfgruber S, Rieger J, Cardozo O, Punz B, Himly M, Stingl A, et al. Antiviral Activity of Zinc Oxide Nanoparticles against SARS-CoV-2. Int J Mol Sci. 2023;24(9).
140. Zhu Y, Chidekel A, Shaffer TH. Cultured human airway epithelial cells (calu-3): a model of human respiratory function, structure, and inflammatory responses. Crit Care Res Pract. 2010;2010.
141. Ammerman NC, Beier-Sexton M, Azad AF. Growth and maintenance of Vero cell lines. Curr Protoc Microbiol. 2008;Appendix 4:Appendix 4E.
142. Beyerstedt S, Casaro EB, Rangel É B. COVID-19: angiotensin-converting enzyme 2 (ACE2) expression and tissue susceptibility to SARS-CoV-2 infection. Eur J Clin Microbiol Infect Dis. 2021;40(5):905-19.
143. McMillian MK, Li L, Parker JB, Patel L, Zhong Z, Gunnett JW, et al. An improved resazurin-based cytotoxicity assay for hepatic cells. Cell Biol Toxicol. 2002;18(3):157-73.
144. Zhang HX, Du GH, Zhang JT. Assay of mitochondrial functions by resazurin in vitro. Acta Pharmacol Sin. 2004;25(3):385-9.
145. Riss TL, Moravec RA. Use of multiple assay endpoints to investigate the effects of incubation time, dose of toxin, and plating density in cell-based cytotoxicity assays. Assay Drug Dev Technol. 2004;2(1):51-62.
146. WHO. Laboratory biosafety guidance related to SARS-CoV-2 2024 [Available from: https://iris.who.int/bitstream/handle/10665/376231/WHO-WHE-EPP-2024.3-eng.pdf?sequence=1.
147. Hernández JM. SARS-CoV-2 risk misclassification explains poor COVID-19 management. The Lancet. 2020;396(10264):1733-4.
148. Loibner M, Langner C, Regitnig P, Gorkiewicz G, Zatloukal K. Biosafety Requirements for Autopsies of Patients with COVID-19: Example of a BSL-3 Autopsy Facility Designed for Highly Pathogenic Agents. Pathobiology. 2021;88(1):37-45.
149. Hardt M, Föderl-Höbenreich E, Freydl S, Kouros A, Loibner M, Zatloukal K. Pre-analytical sample stabilization by different sampling devices for PCR-based COVID-19 diagnostics. N Biotechnol. 2022;70:19-27.
150. Wilhelm J, Vytášek R, Uhlík J, Vajner L. Oxidative Stress in the Developing Rat Brain due to Production of Reactive Oxygen and Nitrogen Species. Oxid Med Cell Longev. 2016;2016:5057610.
151. Sigma-Aldrich. Product Specification Dihydroethidium [Available from: https://www.sigmaaldrich.com/AT/de/product/sial/d7008.
152. Sigma-Aldrich. Product Specification 2′,7′-Dichlorfluorescein-Diacetat [Available from: https://www.sigmaaldrich.com/AT/de/product/sigma/d6883.
153. Wiki AP. BET Theory Wiki Anton Paar [Available from: https://wiki.anton-paar.com/at-de/bet-theorie/.
154. Brunauer S, Emmett PH, Teller E. Adsorption of Gases in Multimolecular Layers. Journal of the American Chemical Society. 1938;60(2):309-19.
155. Lowell S, Shields J, Thomas M, Thommes M. Characterization of Porous Solids and Powders: Surface Area, Pore Size and Density2006.
156. Canta M, Cauda V. The investigation of the parameters affecting the ZnO nanoparticle cytotoxicity behaviour: a tutorial review. Biomater Sci. 2020;8(22):6157-74.

157. El-Beltagi HS, Ragab M, Osman A, El-Masry RA, Alwutayd KM, Althagafi H, et al. Biosynthesis of zinc oxide nanoparticles via neem extract and their anticancer and antibacterial activities. PeerJ. 2024;12:e17588.
158. Xie Y, He Y, Irwin PL, Jin T, Shi X. Antibacterial Activity and Mechanism of Action of Zinc Oxide Nanoparticles against Campylobacter jejuni. Applied and Environmental Microbiology. 2011;77(7):2325-31.
159. Mendes CR, Dilarri G, Forsan CF, Sapata VdMR, Lopes PRM, de Moraes PB, et al. Antibacterial action and target mechanisms of zinc oxide nanoparticles against bacterial pathogens. Scientific Reports. 2022;12(1):2658.
160. Gutiérrez Rodelo C, Salinas RA, Armenta JaimeArmenta E, Armenta S, Galdámez-Martínez A, Castillo-Blum SE, et al. Zinc associated nanomaterials and their intervention in emerging respiratory viruses: Journey to the field of biomedicine and biomaterials. Coord Chem Rev. 2022;457:214402.
161. Moore TL, Rodriguez-Lorenzo L, Hirsch V, Balog S, Urban D, Jud C, et al. Nanoparticle colloidal stability in cell culture media and impact on cellular interactions. Chemical Society Reviews. 2015;44(17):6287-305.
162. Quevedo AC, Guggenheim E, Briffa SM, Adams J, Lofts S, Kwak M, et al. UV-Vis Spectroscopic Characterization of Nanomaterials in Aqueous Media. J Vis Exp. 2021(176).
163. Liu HH, Surawanvijit S, Rallo R, Orkoulas G, Cohen Y. Analysis of nanoparticle agglomeration in aqueous suspensions via constant-number Monte Carlo simulation. Environ Sci Technol. 2011;45(21):9284-92.
164. Anders CB, Chess JJ, Wingett DG, Punnoose A. Serum Proteins Enhance Dispersion Stability and Influence the Cytotoxicity and Dosimetry of ZnO Nanoparticles in Suspension and Adherent Cancer Cell Models. Nanoscale Res Lett. 2015;10(1):448.
165. Singh RP, Sharma K, Mausam K. Dispersion and stability of metal oxide nanoparticles in aqueous suspension: A review. Materials Today: Proceedings. 2020;26:2021-5.
166. Jafarova VN, Orudzhev GS. Structural and electronic properties of ZnO: A first-principles density-functional theory study within LDA(GGA) and LDA(GGA)+U methods. Solid State Communications. 2021;325:114166.
167. Kakaei K, Padervand M, Akinay Y, Dawi EA, Ashames A, Saleem L, et al. Environmental Science and Pollution Research A critical mini-review on challenge of gaseous O 3 toward removal of viral bioaerosols from indoor air based on collision theory. Environmental Science and Pollution Research. 2023;30:3.
168. Correa Sierra CB, Schang LM. On the Sensitivity of the Virion Envelope to Lipid Peroxidation. Microbiol Spectr. 2022;10(5):e0300922.
169. Zhang G, Kuang L, Liu Y, Jiang C, Yang R, Lv Q, et al. Efficient Inactivation of Enveloped Viruses Using a Nanoparticle-Based Photodynamic Method. ACS Applied Nano Materials. 2023;6(19):17647-56.
170. Sifang Steve Z. Variability and Relative Order of Susceptibility of Non-Enveloped Viruses to Chemical Inactivation. In: Raymond WN, Ijaz MK, editors. Disinfection of Viruses. Rijeka: IntechOpen; 2022. p. Ch. 6.
171. Ogochukwu OO, Fabiyi MB, Aworunse OS, Oyewole OA, Isibor PO. Nanoparticle Properties and Characterization. In: Isibor PO, Devi G, Enuneku AA, editors. Environmental Nanotoxicology: Combatting the Minute Contaminants. Cham: Springer Nature Switzerland; 2024. p. 23-40.

172. Hapid M, Setiadhi R. A REVIEW: ZINC AS AN ANTIVIRUS ALTERNATIVE TREATMENT FOR HERPES SIMPLEX VIRUS INFECTION. International Journal of Applied Pharmaceutics. 2022:1-6.
173. Singh P, Ali SW, Kale RD. Antimicrobial Nanomaterials as Advanced Coatings for Self-Sanitizing of Textile Clothing and Personal Protective Equipment. ACS Omega. 2023;8(9):8159-71.
174. Agarwalla S, Singh SK, Ibrahim MA, Noothalapati H, Duraiswamy S. Antimicrobial Coatings. Functional Coatings2024. p. 231-74.
175. Fischer WA, 2nd, Weber D, Wohl DA. Personal Protective Equipment: Protecting Health Care Providers in an Ebola Outbreak. Clin Ther. 2015;37(11):2402-10.
176. Stadnytskyi V, Anfinrud P, Bax A. Breathing, speaking, coughing or sneezing: What drives transmission of SARS-CoV-2? Journal of Internal Medicine. 2021;290(5):1010-27.
177. Wang CC, Prather KA, Sznitman J, Jimenez JL, Lakdawala SS, Tufekci Z, et al. Airborne transmission of respiratory viruses. Science. 2021;373(6558).
178. Božič A, Kanduč M. Relative humidity in droplet and airborne transmission of disease. J Biol Phys. 2021;47(1):1-29.
179. Verheyen CA, Bourouiba L. Associations between indoor relative humidity and global COVID-19 outcomes. J R Soc Interface. 2022;19(196):20210865.
180. Guo C, Bo Y, Lin C, Li HB, Zeng Y, Zhang Y, et al. Meteorological factors and COVID-19 incidence in 190 countries: An observational study. Sci Total Environ. 2021;757:143783.
181. Morris DH, Yinda KC, Gamble A, Rossine FW, Huang Q, Bushmaker T, et al. Mechanistic theory predicts the effects of temperature and humidity on inactivation of SARS-CoV-2 and other enveloped viruses. Elife. 2021;10.
182. Dhawan S, Biswas P. Aerosol Dynamics Model for Estimating the Risk from Short-Range Airborne Transmission and Inhalation of Expiratory Droplets of SARS-CoV-2. Environ Sci Technol. 2021;55(13):8987-99.
183. Mofidfar M, Mehrgardi MA, Xia Y, Zare RN. Dependence on relative humidity in the formation of reactive oxygen species in water droplets. Proceedings of the National Academy of Sciences. 2024;121(12):e2315940121.